國立臺灣大學電機資訊學院電機工程學系

碩士論文

Department of Electrical Engineering
College of Electrical Engineering and Computer Science
National Taiwan University
Master Thesis

使用低成本雷射測距儀與即時組織硬度估測之適應性軌跡規劃系統於機器人按摩之研究

Adaptive Trajectory Generation of Robotics Therapeutic Massage Using Low-Cost Laser Range Finder with In-Situ Tissue Stiffness Estimation

唐莉彤

Li-Tung Tang

指導教授：羅仁權 博士

Advisor: Ren C. Luo, Ph.D.

中華民國 106 年 7 月

July 2017

doi:10.6342/NTU201703367

誌謝

就讀碩士班這兩年是我人生裡一段美好的回憶。雖然一路走來不易，但還好有大家的支持與陪伴我才能有今日的成就。感謝父母親的栽培教誨、支持鼓勵，讓我能夠全心全意奮力一搏，專注於我喜愛的領域。 特別感謝指導教授羅仁權老師讓我有學習的機會。老師經常陪著我們熬夜，給我們指點迷津，每一次的實驗瓶頸，每一個文法的迷惘，都謝謝有老師及時的援手。當我感到疲憊，沒有堅持下去的動力時，只要想到老師的拼勁，就讓我打包心情，重新面對挑戰。 感謝老師提供我們豐富的資源及在研究過程中的教導。在兩年的碩士生涯中，從老師身上學到許多，老師充分地展現出國際級專家學者的風範與視野，不僅帶領我們探索學術知識上的深度與廣度，在待人處事方面，老師更是教給我們許多社會上應對進退的準則，期望我們成為均衡發展的人才，這一切都使我獲益良多。感謝康仕仲老師以及鄒杰炯老師百忙之中擔任我的口試委員，並給予我的論文諸多的建議及指教。回想兩年前，剛決定從光電領域跨到電機時，心中既期待又對未知的未來感到些許徬徨。一開始對程式不太熟悉的我，經過兩年在實驗室的學習，成長進步很多。在實驗室不僅培養軟體相關能力，也有許多機會接觸硬體，擁有軟硬體整合的能力，是相當難得的體驗也是此實驗室給我最大的禮物。謝謝我同窗兩年的同學，感謝你們在我人生迷惘、情緒低落時，給我鼓勵，帶給我無限的希望，也對於我的研究提供了許多好的建議與想法。俊豪、晴岡、柏凱、李晟、靖霖、達方，謝謝你們在一起修課時幫我解答問題。謝謝當時一起比賽的長鈞、孟勳、仲凱，謝謝你們給我一個這麼棒的經驗，也讓我更加確信團隊合作的重要，創造了寶貴的回憶。謝謝按摩機器人組的凱鈞、昱佑，謝謝你們總是在研究上給予我幫助，一起做實驗一起討論，給予我許多技術上的教學以及在面臨低潮時鼓勵我，成為我最佳的夥伴。同時我也感謝實驗室學弟妹，總是義不容辭的協助我做實驗，幫忙舉辦實驗室的活動。也感謝實驗室的學長，在研究上有相關問題，總是熱心回答並提供許多寶貴的建議與經驗，解決我在研究路上有遇到的瓶頸。

能完成這篇論文，我要感謝生命中的每一個人，真的非常謝謝你們。

唐莉彤 謹誌

一百零六年七月

doi:10.6342/NTU201703367

中文摘要

隨著人口老化與人們對生活品質的要求提升，服務與醫療照護型機器人逐漸走入我們的生活中，具有相當大的市場。現代人壓力大作息不正常，常常造成肩背痠痛，而按摩為一種常見的舒緩方式，其不只幫助人們放鬆也可被視為是一種治療。若機器人可被應用於按摩上，不僅能解決醫療人力不足的問題也可增進醫療品質。

本篇論文以雙手臂機器人於肩背按摩為主軸，發展出一套完整的自動化按摩流程。該流程包含使用自製的低成本雷射測距儀產生專屬個人的適應性按摩軌跡，以及加入即時組織估測系統使機器人在按摩過程中能自行估測被按摩部位組織的厚度與硬度。按摩前置部分。在以往，機器人的按摩軌跡大多透過教導的方式或是利用使用者介面來產生，此作法耗時又耗費人力。而在此我們使用自製低成本的 3D 雷射測距儀搭配現有的變形演算法找出人體肩部與背部的按摩軌跡。該雷射測距儀具有與市售產品相當的精度且售價只需一般產品十分之一不到的價格。我們利用此雷射測距儀掃描人體以產生背部的立體模型，並將該模型與預先建立已具有標準按摩軌跡的模型做映射來找出專屬於每個人的按摩軌跡。實驗結果顯示此方法所找出的按摩指壓點與專業按摩師所認可的指壓點平均距離誤差為 1 公分，產生軌跡的的時間也只需教導方式的一半。在按摩的過程中，則加入了即時組織估測系統。我們透過 7 軸手臂等速按壓人體背部找出皮膚組織力量與深度的曲線，將人體的皮膚特性模組化為一正切函數。實驗中機器人雙手前端裝有力/力矩感測器，可即時量測按摩器具與被按摩者間所受的力。我們將此力與機器人末端的移動做為估測演算法中訊號的輸出與輸入，並藉由遞迴最小平方法加上遺忘因子在按摩中即時找出函數當中的參數以估測組織的軟硬。該實驗分為模擬與實際量測。模擬結果顯示該演算法可在 20 秒內估測出組織的特性。而在實際量測中，機器人對不同體型的受測者進行按壓按摩並估測骨頭周遭、硬肌肉、軟肌肉的組織的特性。實驗結果顯示其可在 1 分鐘內估測出組織的特性且其結果與先前模組化的軟組織模型趨勢相同並有潛力可做為判斷被按摩者身體狀況的標準。

關鍵字: 雙手臂機器人、低成本雷射測距儀、適應性按摩軌跡規劃、即時組織硬度估測

doi:10.6342/NTU201703367

ABSTRACT

With the increasing rate of the elderly and the promotion of life quality, service robot and health care robot play important roles in our life and have huge market potential. Modern people usually suffer shoulder and back pain because of the pressure and irregular routine. Massage, a common way to alleviate the pain, can help people relax as a therapy. If robots are able to be supplied for massage, it can solve the shortage of medical human and promote the quality of therapy. In this thesis, we develop a complete automated procedure on dual arm robot for shoulder and back massage application. It contains using self-developed low-cost laser range finder (LRF) to generate adaptive massage trajectory which is individual person specific and implementing in-situ tissue stiffness estimation to make robot can figure out the characteristics of patient's soft tissue during massage. In pre-massage procedure, prior researches often apply teach and play or user interface to generating massage trajectory and these techniques are time-consuming and laborious. Here we use a 3D low-cost LRF made by ourselves and existing morphing algorithm to find the trajectory of shoulder and back massage. This LRF has the comparable performance as commercial products and its cost is less than 10% of the cost of general products. We use the LRF to scan human's back and generate a 3D model. Then the standard model which has the massage trajectory we decide in advance will be mapped on the model of human's back to generate the massage trajectory for different people with different size. The experimental results demonstrate that the average distance error between the acupressure points indicated by our method and the acupressure points defined by the massage therapist is 1cm and our method can save more than half the time needed with teach and play. During the massage, we add an in-situ tissue stiffness estimation. We

doi:10.6342/NTU201703367

use a 7 DoF arm to find the indentation-force curve of soft tissue and model the characteristics of soft tissue as a tangent function. The wrists of the robot are equipped with force/torque sensors which can detect the force between massage tools and the patient. We take this force and the movement of robot manipulator as output and input signals and apply the recursive modified least-squares algorithm with forgetting factor to find the parameters of the function and estimate the hardness and thickness of tissue. From simulation results, the algorithm can estimate the characteristics of soft tissue in 20s. In the experiment, the robot executes pressing massage on different subjects with different body size and finds the characteristics of three types of soft tissues, which are the tissue that covers bony area, hard muscle, and soft muscle. From experimental results, it can estimate the characteristics of soft tissue in 1 minute. The estimation results have the same trend as the model of soft tissue we build previously and have the potential to be the judging criteria of body condition.

Keywords: dual arm robot, low-cost laser range finder, adaptive massage trajectory generation, in-situ tissue stiffness estimation

doi:10.6342/NTU201703367

TABLE OF CONTENTS

doi:10.6342/NTU201703367

doi:10.6342/NTU201703367

LIST OF FIGURES

doi:10.6342/NTU201703367

doi:10.6342/NTU201703367

LIST OF TABLES

doi:10.6342/NTU201703367

Chapter 1 Introduction

1.1 Motivation

Health care robots play important roles for humans with the rapid increase of the elderly population and an acute shortage of nurses. They have huge potential for improving quality of life by automating time-consuming and laborious medical procedures. There are different types of health care robots that have been proposed such as the nursing-care assistant robot RIBA [1], a mobility assistant robot [2], and the domestic health assistant robot MAX [3]. Massage is a non-invasive and effective therapy. It has lots of befits include pain relief, reduced trait anxiety and depression, and temporarily reduced blood pressure and heart rate. However, it is time-consuming and laborious. Therefore, robotics therapeutic massage is highly valued recently in the field of health care robots which can provide more diversified massage techniques, has wider workspace, and more closely meets the needs of users than a standard massage chair.

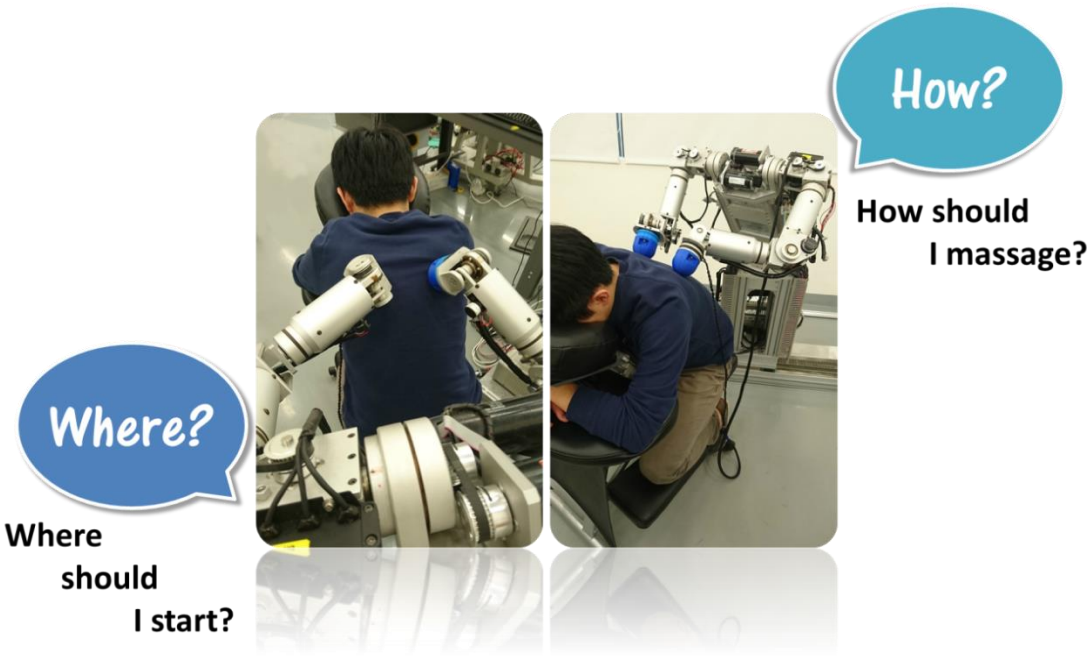

Fig. 1-1 The dual arm robot for massage application.

doi:10.6342/NTU201703367

The dual arm robot for massage application is shown in Fig. 1-1. It is developed with three main topics (Fig. 1-2): massage trajectory planning, control strategy implementation, and effectiveness evaluation. Several studies have focused on the latter two parts. Huang et al. [4] [5] designed an anthropomorphic soft arm with integrated elastic joints and considered its contact dynamics for promoting quality of massage. Ando et al. [6] evaluated the relaxation effect of the head massage robot with bio signals. Our previous works have also discussed the impedance control of the multi-finger robot [7] and developed a robotics therapeutic massage evaluation system [8] [9] by using electromyography (EMG) and electroencephalogram (EEG) signals.

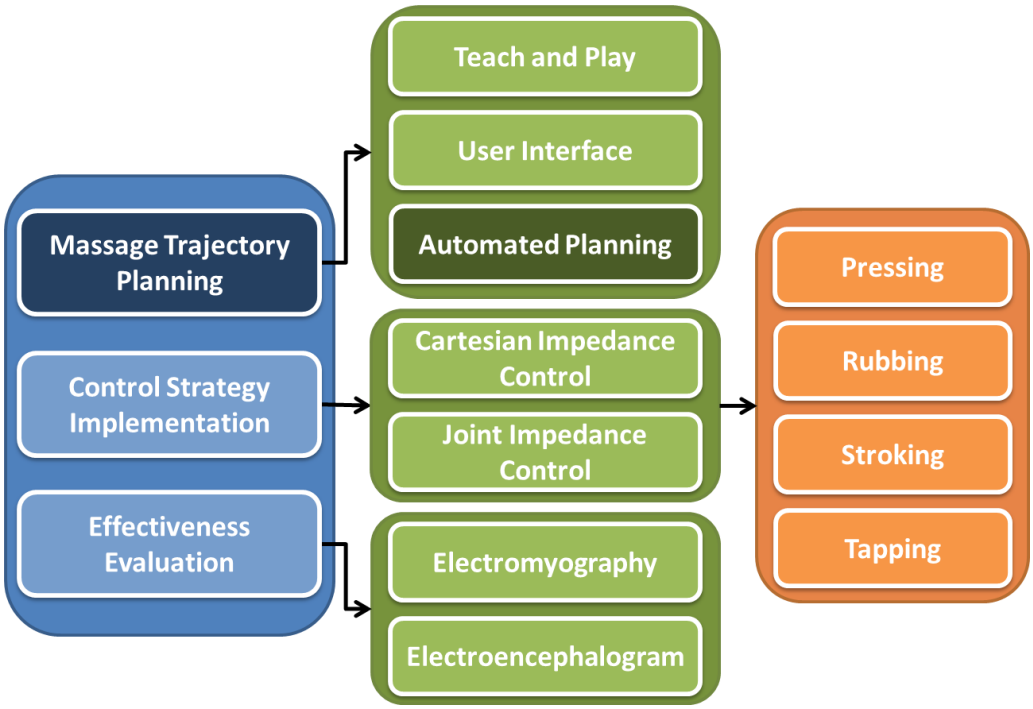

Fig. 1-2 The massage functions of the dual arm robot.

There have been papers discussing massage trajectory planning, but they often generate the trajectories through teach and play or user interface. They are not an automated process and unsuitable for different body shapes. It will cause a lot of inconvenience and it puts the cart before the horse. Like real masseur, the robot needs to

doi:10.6342/NTU201703367

know “where” it should start to massage by itself. It should autonomously generate suitable massage trajectory for different people. To solve this problem, sensor is indispensable. However, sensor is another problem for robotics massage.

There are many sensors such as sonar, IR sensors, and Laser Range Finders (LRFs) can be used, whereas LRFs have the higher potential than other sensors due to their higher accuracy with fine angular and distance resolution and more dense distance measurements. The stumbling block to using LRF in general applications is the cost. The main reasons of the high cost are the optical components and the scanning mirrors which are very fragile and expensive. Although many commercial products from famous company such as SICK and Hokuyo (Fig. 1-3) have been fully developed, the cost of them about several thousand US dollars still keeps them from common use. Therefore, we have been finding a cheaper and more available way to make LRFs.

Fig. 1-3 The commercial LRF products. Left: SICK Right: Hokuyo

Although the robot can know where it needs to massage by sensors, it still needs to know “how” it should massage. For general masseur, they can know what kind of soft tissue they are massaging when they touch them and even can figure out the body condition of patients. Then they will use this information to determine the massage strategy such as massage duration and massage techniques. To provide patients more

doi:10.6342/NTU201703367

comfortable and friendlier service, robot should have the same ability as real masseur. Therefore, how to interact with soft tissue becomes important issue for robotics therapeutic massage. If we want the robot to achieve the goal, it needs to understand the characteristics of soft tissue and estimate the characteristics of patient's soft tissue during massage. Other advantages of this ability are that the robot can adjust the control strategies according to tissue stiffness to make the control system more stable and it is able to evaluate the massage effectiveness by comparing the tissue stiffness before and after the massage.

Sum up the above perspectives, there are two problems to be solved. First one is make the robot autonomously generate adaptive massage trajectory by using not expensive sensor. Second one is let the robot can figure out the characteristics of patient's soft tissue during massage.

1.2 Related Work

1.2.1 Massage Trajectory Planning

Teach and Play): Jones et al [10] developed a robotic system to provide basic massage manipulations for medical therapy by employed a PUMA 562 robot. For trajectory generation, the trajectory is generated based on 4 data at the patient's left and right shoulders and left and right points on the waist which are taught by masseur in Cartesian space. In order to obtain desired Cartesian trajectory, they use inverse kinematics and Jacobian matrix to get a desired sequence of joint positions and velocities. King et al [11] developed a system making the robot autonomously perform bed baths for patient hygiene. They acquired the spatial data of patients from a Hokuyo laser range finder and created a selection interface. The operator can use mouse to select

doi:10.6342/NTU201703367

2 points and these 2 points will form the diagonal corners of a rectangular box which the operator wants robot to clean. They evaluate the performance of the system by making the robot remove a certain area of debris on human skin. The experimental results show that the robot can remove 96% of the debris on 4 parts of the limbs. Lu et al [12] designed a Chinese medical massage system which can record the acupressure points of patients by affixing color labels on back. Although the masseur can teach the robot the positon of acupressure points on human back, these points may be changed during massage and the robot will touch the wrong place. To avoid that happening, they affix the color labels on back as marks. When the robot executes massage, it can use camera to check the position of acupressure points at any time. Peng et al [13] also adopted similar method to record the acupressure points by recognizing the position of the masseur's finger.

Automated Massage Trajectory Planning): Wei et al [14] presented a foot massage robot which can reproduce the expert techniques of Chinese massage. For trajectory planning, they first measure the foot size to get patient's pelma contours and find the coarse position of acupoints of pelmas by using a knowledge-based predictive model which is based on the feature points of foot. Then they adopt reinforcement learning optimization to correct the errors calculated through the prediction model and get the fine position of acupoints. Chen et al [15] developed a 2 DoF massaging robot prototype: Massagebot. It can realize massage by scratching and shaking on user's back. In order to get better efficacy, they proposed an algorithm which combine SOM (Self-organizing Feature Map) neural networks, image processing and pattern recognition to simplify acupuncture points and make the robot through the path which has most of acupressure points. The method we proposed previously [16] was based on

doi:10.6342/NTU201703367

the human pose recognition methodology provided by [17]. We extracted point cloud data of human body shape from Kinect and estimated the frontal and sagittal planes by RANSC (RANdom Sample Consensus) algorithm to plan the massage trajectories for different shapes of a human body. Since it only depends on the planes of human body, the accuracy is not enough and the effectiveness cannot be proved.

1.2.2 Laser Range Finder

Konolige et al. [18] developed a laser distance sensor based on triangulation principle (Fig. 1-4(Left)). They adopted a point laser and low-cost CMOS imager as the emitter and the receiver to build an innovative laser point sensor module. Its cost is about $30 and it has the accurate range measurements at 6m with less than 3cm errors. This approach can only get 2D information with one scan because of the point laser. Chen et al. [19] proposed an ultra-tiny line laser range sensor based on the time-of-flight principle (Fig. 1-4(Right)). Its size is only 35mm×27mm×30mm which makes them possible for smaller robotics applications and the cost is $150 for prototype. The disadvantage of it is its measurable range is too short.

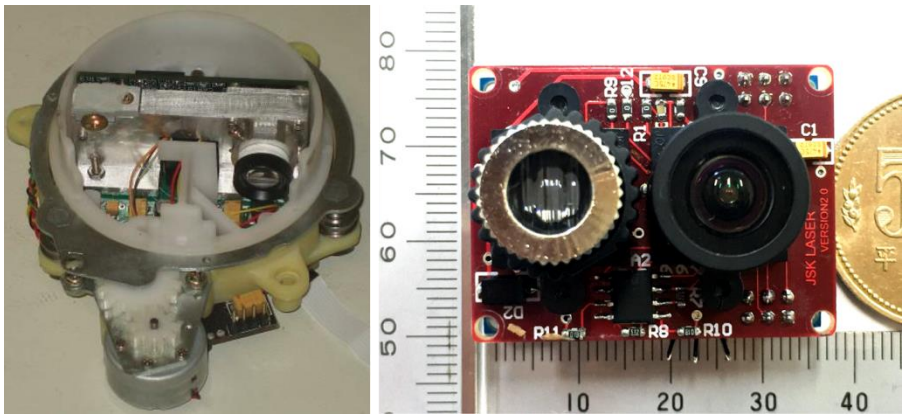

Fig. 1-4 The laser distance sensors developed from related work. Left: LRF based on triangulation. Right: Tiny LRF based on time-of-flight (TOF).

doi:10.6342/NTU201703367

1.2.3 Interaction with Soft Tissue

Modeling of Soft Tissue): As far back as 1996, Chen et al [20] believe that quantitative measurement of tissue elasticity is helpful to numerous potential clinical applications. They built a 1D ultrasound elasticity measurement system to investigate the elasticity of muscle and liver and compared the accuracy and consistency with mechanical measurements. They found that stress-strain curves of soft tissue have exponential shapes. Hu et al [21] also deduced the same characteristic of soft tissue. They measured the mechanical properties of living tissue of person's arm by a 4 DoF massage robot arm. There is a 6mm diameter tip mounted on the force sensor of robot arm. The tip obtains the external force on human tissue by moving at constant velocity to compress person's arm. The experimental results have the same trend as [20]. Moreover, they found that different velocity will not affect the results. Yeh et al [22] proposed a modified contact model that uses contact radius and contact force to estimate the elastic modulus of objects and proposed an image-assisted measuring system which adopts CCD camera to detect the contact radius and the contact force is extracted by tactile sensor. This method increases the accuracy of estimation. Yakovenko et al [23] numerically figured out the model of the three-layer tissue, which simulates skin, muscle, and bone, and used the results to estimate the contact and internal stresses between the element of the medical robot and soft tissue. The algorithm they proposed reduces much time for signal and data processing while does not lead to loss of model adequacy.

Integration with Control System): Golovin et al [24] [25] consider that training by demonstration in robotics is more natural for physician than training of force points using the manual by physician. The massage robot imitates the movement of masseur

doi:10.6342/NTU201703367

and recorded the force exerted on soft tissue by masseur through demonstration. In the free space, it only needs to care about the movement. But during massage, it should consider the interaction with soft tissue. In their model, they add the factor of the reaction force of soft tissue to make the robot can record the true force exerted by masseur and successfully reproduce the action of massage. Ott et al [26] [27] developed a hybrid system for impedance and admittance control. They found that impedance control is suitable for interactions with stiff tissue and admittance control is suitable for interactions with soft tissue, so they alternated the controller between these two control methods with different tissue stiffness which are known in advance. This research makes us understand the interaction between control and soft tissue better. Mouri et al [28] proposed an intelligent massage control system. They identified the characteristic of human skin muscle through robot perception of impedance control to determine the parameters of the controller. In the experiments, they estimated the suitable impedance control parameters for a soft tissue and a hard muscle. It successfully helped us handle the control strategy with soft and hard muscle.

1.3 Objective

In this thesis, there are two main issues to be solved. First one is make the robot can autonomously generate adaptive massage trajectory which is individual person specific by using a low-cost sensor. We aim to develop a low-cost laser range finder (LRF) which has lots of advantages than other sensors and we will focus on upper back massage which is the most common way in massage. Second one is to figure out the characteristics of soft tissue and let the robot can estimate the characteristics of patient's soft tissue during massage. We will explore a more intuitive model than previous works and propose a method that can online estimate the characteristics of soft tissue.

doi:10.6342/NTU201703367

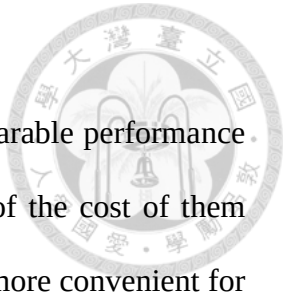

Several sub-objectives of this thesis are presented as follow:

1. Develop a low-cost laser range finder which has the comparable performance with commercial products but the cost is less than 10% of the cost of them and make it can get 3D model with a single scan which is more convenient for massage trajectory planning.
2. Propose a method that can generate adaptive massage trajectory which is suitable for different people with different body size and individual person specific according to human back feature.
3. Apply the LRF and adaptive massage trajectory generation we propose to robotics therapeutic massage, including upper back massage and full body massage.
4. Explore the characteristics of soft tissue and propose a more intuitive model of soft tissue than previous work which can indicate the hardness and thickness of soft tissue.
5. Propose a method that can estimate the characteristics of patient's soft tissue during massage by using the information from the reaction force by patient's soft tissue and the movement of the robot manipulator.

1.4 Thesis Organization

The thesis is organized and described as follow: Chapter 1 discloses the motivation, related work, and the objective of this thesis. Chapter 2 gives a hardware and soft system description of the dual arm robot developed in our lab for robotics therapeutic massage. The control techniques of the dual arm robot, including different massage techniques are illustrated in Chapter 3. The hardware and software system and the laser module of the self-developed LRF are described in Chapter 4. The performance of the

doi:10.6342/NTU201703367

LRF compared with commercial product is also presented in that chapter. Chapter 5 presents the methodology we propose in this thesis for adaptive massage trajectory generation which is based on morphing algorithm and medical knowledge, the experimental results are presented as well. Chapter 6 illustrates the intuitive model of soft tissue and describes the in-situ tissue stiffness estimation based on adaptive law for physical human-robot interaction; the experimental results of estimation are also presented. Finally, Chapter 7 concludes our works and discloses the future work in this thesis.

doi:10.6342/NTU201703367

Chapter 2 System Overview

In this chapter, we disclose the hardware and software system of the dual arm robot developed in our lab for robotics therapeutic massage. We first give a system overview of the dual arm robot. Then we describe the hardware system and kinematics of the robot arm. Finally, the system structure and the software are presented.

2.1 Anthropomorphic Dual Arm Robot

Fig. 2-1 shows the anthropomorphic dual arm robot system developed in NTU-iCeiRA Lab. It has 6 DoFs on each arm (3 rotational-DoFs in shoulder, 1 rotational-DoF in elbow, and 2 rotational-DoFs in wrist) and 1 DoF on the bottom with a linear motor for mobility. There are 13 DoFs in total.

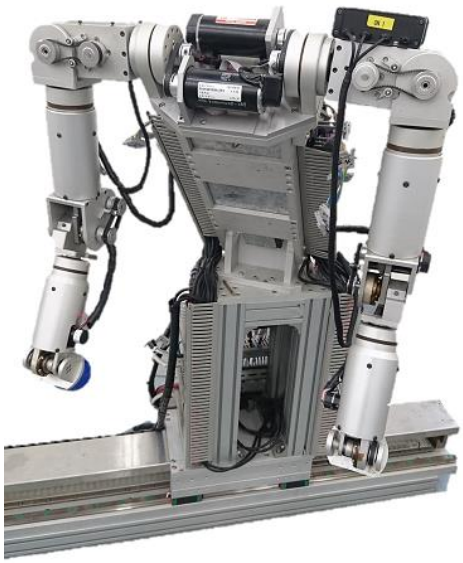

Fig. 2-1 The anthropomorphic dual arm robot developed in NTU-iCeiRA Lab.

It is equipped with a sphere-shaped end-effector for performing a variety of massage techniques and a force/torque sensor on each wrist to measure the interactional force between the end effector and soft tissue of patient during massage. The torso is bended forward by 45 degrees to get a larger workspace in front of the robot. Its control

doi:10.6342/NTU201703367

system is based on the real time operating system RTX on window PC.

We are also developing another anthropomorphic dual arm robot for health-care which is shown in Fig. 2-2. It has more DoFs which can performance more complex tasks not only massage. It has 7 DoFs on each arm, 3 DoFs on waist, 2 DoFs on head equipped with tablet for human-robot interaction, and 4 DoFs on the bottom which has 4 Omni-directional wheels for mobility. There are 23 DoFs in total. The end effector of the robot can be altered to accommodate different massage techniques to achieve the optimal effect.

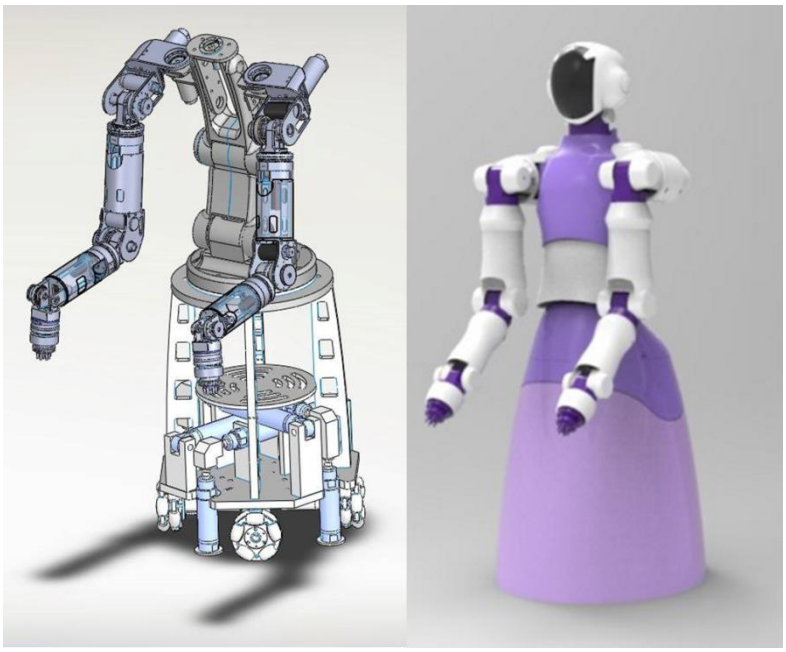

Fig. 2-2 The anthropomorphic dual arm robot which we are developing.

2.2 Hardware System of Robot Arm

Fig. 2-3 shows the mechanic design of the robot arm. The length of each arm is about 60 cm. Its controllers are put in the torso. We take aluminum alloy as the material of the robot arm which can reduce its weight. Its specifications are presented in Table 2-1.

doi:10.6342/NTU201703367

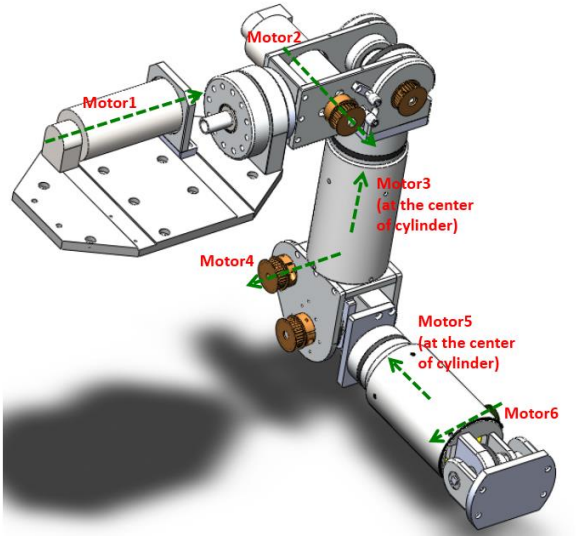

Fig. 2-3 The mechanic design of the robot arm.

Degree of Freedom (DoF)	Length	Weight
Shoulder: 3 DoFs	Shoulder: 115 mm	Shoulder: 2.3 kg
	Upper arm: 300 mm	Upper arm: 3.3 kg
Elbow: 1 DoF	Forearm: 300 mm	Forearm: 2.2 kg
	Diameter: 100 mm	Fist: 0.5 kg
Wrist: 2 DoFs	Total length: 600 mm	Total weight: 8.3 kg

Table 2-1 The specifications of the robot arm.

Each joint of the robot arm is actuated by a DC brush servo motor (Fig. 2-4(Left)) from Maxon. For massage application, we need a driver which can provide torque mode to make motor output desired torque and we also need a reduction gear which can reduce the rotational speed and transfer the energy to torque output to let motor has higher output torque. To satisfy our requirement, we take Maxon servo amplifier (Fig. 2-4(Right)) as the driver and adopt Harmonic Drive as the reduction gear. Compare to traditional reduction gear, Harmonic Drive has higher compactness, lighter weight and

doi:10.6342/NTU201703367

higher gear ratios. Their specifications are shown in Table 2-2.

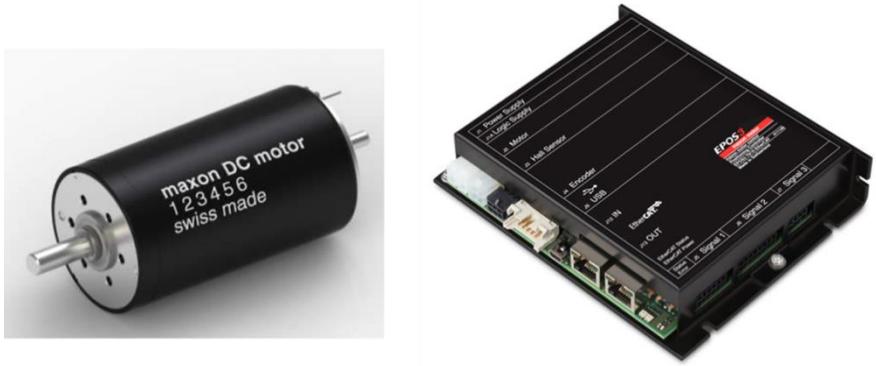

Fig. 2-4 The motor and the driver used in each joint.

Joint	Motor Type	Nominal Speed (rpm)	Nominal Torque (mNm)	Nominal Current (A)	Torque Constant (mNm/A)	Harmonic Drive Type	Gear Ratio
Shoulder	RE-50	5540	354	9.15	39.6	CSD-17-50	50
	RE-50	5540	354	9.15	39.6	CSD-17-50	50
	RE-40	6930	170	5.77	30.2	CSD-20-50	50
Elbow	RE-40	6930	170	5.77	30.2	CSD-17-50	50
Wrist	RE-25	8360	26.7	1.17	23.4	CSD-14-100	100
	RE-25	8360	26.7	1.17	23.4	CSD-14-100	100

Table 2-2 The specifications of each joint.

The mechanism of Harmonic Drive is shown in Fig. 2-5 [29]. It has 3 basic components: a wave generator (green), a flex spline (red), and a circular spline (blue). Its theory is based on elastic dynamics and utilizes the flexibility of metal. It assumes that the wave generator is the input rotation. The key point of the mechanism is that the flex spline has fewer teeth than the circular spline has so that the flex spline is required to rotate a slight amount backward relative to the circular spline. Thus the rotation

doi:10.6342/NTU201703367

action of the wave generator brings on a much slower rotation of the flex spline in the opposite direction.

The gearing reduction ratio can be calculated by the number of teeth on each gear as:

$$reduction\ ratio = \frac{flex\ spline\ teeth - circular\ spline\ teeth}{flex\ spline\ teeth} \quad (2.1)$$

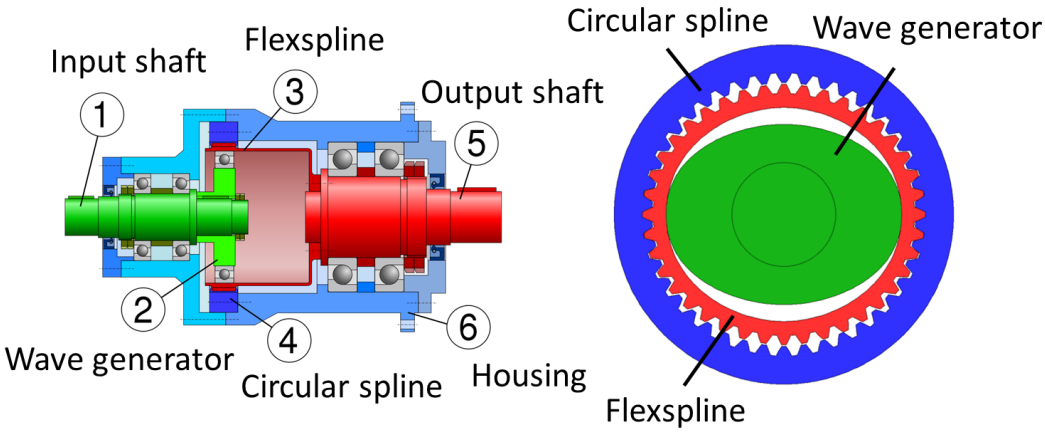

Fig. 2-5 The mechanism of Harmonic Drive.

Fig. 2-6 The 6-axis F/T sensor is mounted on the wrist of each robot arm.

In order to measure the interactional force between the end effector and soft tissue of patient during massage for physical human-robot interaction and evaluating the quality of massage, the 6-axis force/torque sensor (HEX-70-CE-2000N) made by Optoforce is amounted on the wrist of each robot arm as shown in Fig. 2-6. This sensor

doi:10.6342/NTU201703367

can measure 3 axis forces (x, y, z) and 3 axis torques (roll, pitch, yaw). Its diameter is 70mm and its height is 20mm. The maximum output force of the end-effector is about 140N.

2.3 Kinematics of Robot Arm

For any application of robot, we need to know the pose of the end-effector in Cartesian space and the angle of each joint in joint space which can be used to make the robot execute the behavior we want. Therefore, we use Denavit-Hartenberg (D-H) convention, which is a general principle to describe the relationship between every link coordinate system, to present the position and orientation of end-effector by a 4×4 homogeneous transformation matrix.

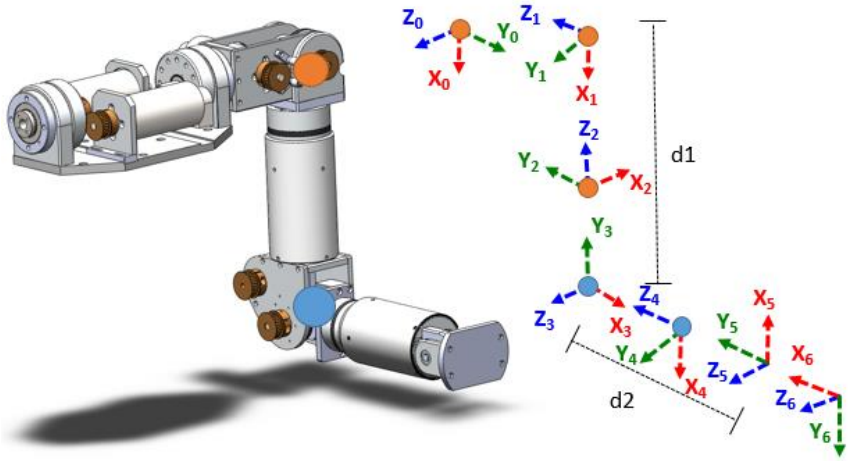

Fig. 2-7 Link coordinate systems of the 6-DOF robot arm.

Fig. 2-7 shows the link coordinate systems of the robot arm and its D-H parameters are presented in Table 2-3. After we determine the reference frame and the D-H parameters, we can calculate the transformation matrix which presents the relationship between the pose (position and orientation) of the end-effector and the angle of each joint.

doi:10.6342/NTU201703367

Joint i	θ_i	d_i	α_i	a_i
1	θ_1	0	900	0
2	θ_2-900	0	900	0
3	θ_3-900	d1=-300mm	900	0
4	θ_4-900	0	900	0
5	θ_5-1800	d2=-300mm	900	0
6	θ_6-900	0	00	a=100mm

Table 2-3 D-H parameters of the 6-DOF robot arm.

The transformation matrix from $i-1$ coordinate to i coordinate can be calculated as:

$$ {}^{i-1}_{i}T = \begin{bmatrix} cos\theta_i & -cos\alpha_i sin\theta_i & sin\alpha_i sin\theta_i & a_i cos\theta_i \\ sin\theta_i & cos\alpha_i cos\theta_i & -sin\alpha_i cos\theta_i & a_i sin\theta_i \\ 0 & sin\alpha_i & cos\alpha_i & d_i \\ 0 & 0 & 0 & 1 \end{bmatrix} \quad (2.2) $$

Then the pose of the end-effector can be expressed by base frame through six transformation matrix as (2.3).

$$ {}^{0}_{6}T = {}^{0}_{1}T\,{}^{1}_{2}T\,{}^{2}_{3}T\,{}^{3}_{4}T\,{}^{4}_{5}T\,{}^{5}_{6}T = \begin{bmatrix} {}^{0}_{6}R & {}^{0}_{6}P \\ 0 & 1 \end{bmatrix} \quad (2.3) $$

where ${}^{0}_{6}R$ is a rotation matrix and ${}^{0}_{6}P$ is the position vector. Each matrix represents each link coordinate system at the joint with respect to the previous link coordinate system.

2.4 System Architecture

The system architecture of the dual arm robot is shown in Fig. 2-8. To give patient a good massage experience, the force acted on patient is considered as first priority instead of the accuracy of position. So we adopt the torque control rather than implement the position control. The control algorithms are coded in PC and the torque

doi:10.6342/NTU201703367

output of the motors are monitored by servo drivers. The servo drivers will send corresponding current to motors to let the motors output desired torque. But these servo drivers only can accept analog voltage as input signals, there is the difficulty with communication between PC and servo drivers. Therefore, we adopt a motion control card to solve this problem. The motion control card we use is Intelligent Motion control Platform (IMP, ITRI) developed by Industrial Technology Research Institute. It main purposes are to convert the digital signals from PC to the analog voltage signals which can be compatible for servo drivers and convert the position information of encoders to the signals which can be interpretable by PC. The specifications of the IMP card are illustrated in Table 2-4.

CPU	400MHz 32bit 7-stage pipeline RISC 32KB D Cache / 32KB I Cache
FPU	100MHz 5-stage double precision FPU with 2.0 MFLOPS/MHz
PCI-Bridge	33MHz 32bits 132MB/sec
DDR-Controller	100MHz DDR 128MB
Ethernet-Controller	10/100Mbps
UART	115200bps
Pulse-Generator	8 sets of 25MHz, function of DDA
Encoder	8 sets of 32bit 4MHz differential input +digital filter
DAC	8 sets of 16bits -10V~10V
ADC	8 sets of 14bits 116ksps -5V~5V(Bipolar)0~10V(Unipolar)

Table 2-4 The specifications of IMP card.

doi:10.6342/NTU201703367

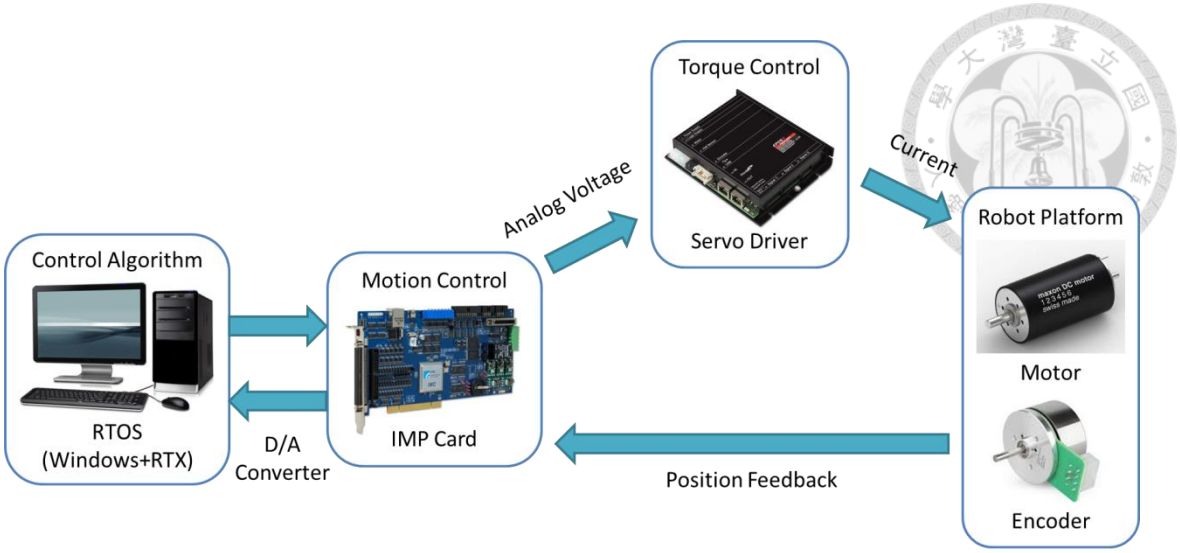

Fig. 2-8 The system architecture of the dual arm robot.

Microsoft Windows is the most widely used operating system in the world. However, there is a crucial issue of this system for control. Because it is a multitasking operating system which has ability to run more than one thread in the background, it cannot has same period of every CPU interrupt and this unbalanced sampling period will cause the command of control can be correctly computed.

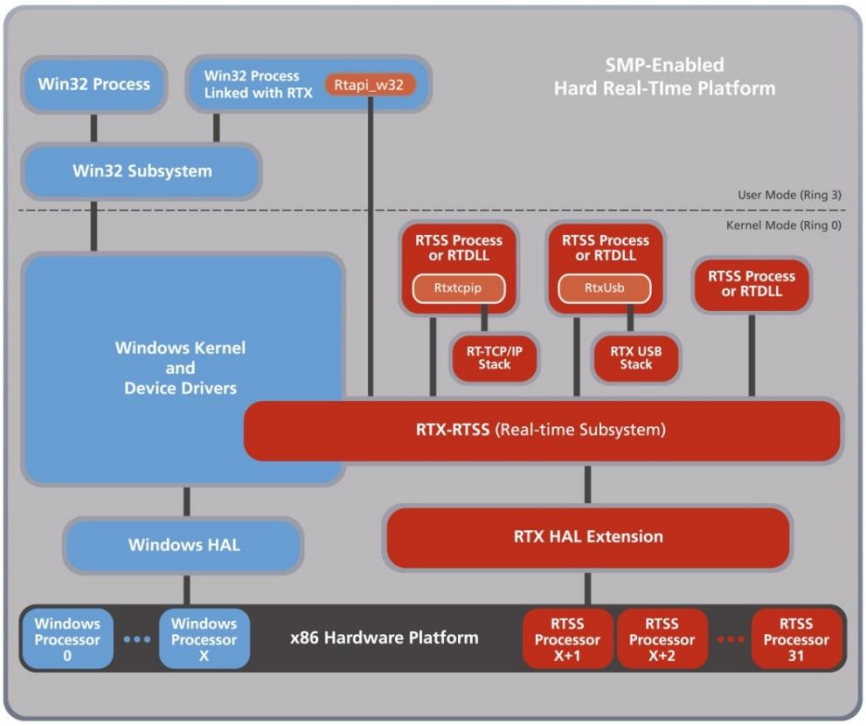

Fig. 2-9 RTX real-time platform.

doi:10.6342/NTU201703367

RTX2016 (IntervalZero) [30], a hard real-time software released by IntervalZero, has the ability to transform Microsoft Windows into a real-time operating system. It can divide the multiple cores into the part for real-time processing and the part for general purpose processing as shown in Fig. 2-9 where some cores are for Microsoft Windows and other cores are for RTX real-time signal processing function. Its memory is shared through the same high-speed bus which allows for data sharing and inter-processor communications. Therefore, the robot control system can be implemented in an environment without unbalanced sampling period.

2.5 Software Architecture

Fig. 2-10 presents the software architecture of the dual arm robot. All the control algorithms are written in C++ language under Microsoft Visual Studio 2010. There are many useful open source libraries can be used for robotic kinematics and dynamics such as Robotics Library and Eigen. The robot parameters defined in hardware layer and the functions of communication interface are to send torque command and receive encoder feedback. The information of tool center point (TCP) can be calculated through forward kinematics in basic utilities and the dynamics which is important for robot control is deal with in this layer as well. Based on the basic utilities, Cartesian space impedance control and joint space control are able to be implemented in control layer. These 3 layers are updated every 1ms for real time control. Finally, the massage techniques and intuitive teach are achieved by application layer. The information about the robot state and the values of each joint is displayed with 100ms timer.

doi:10.6342/NTU201703367

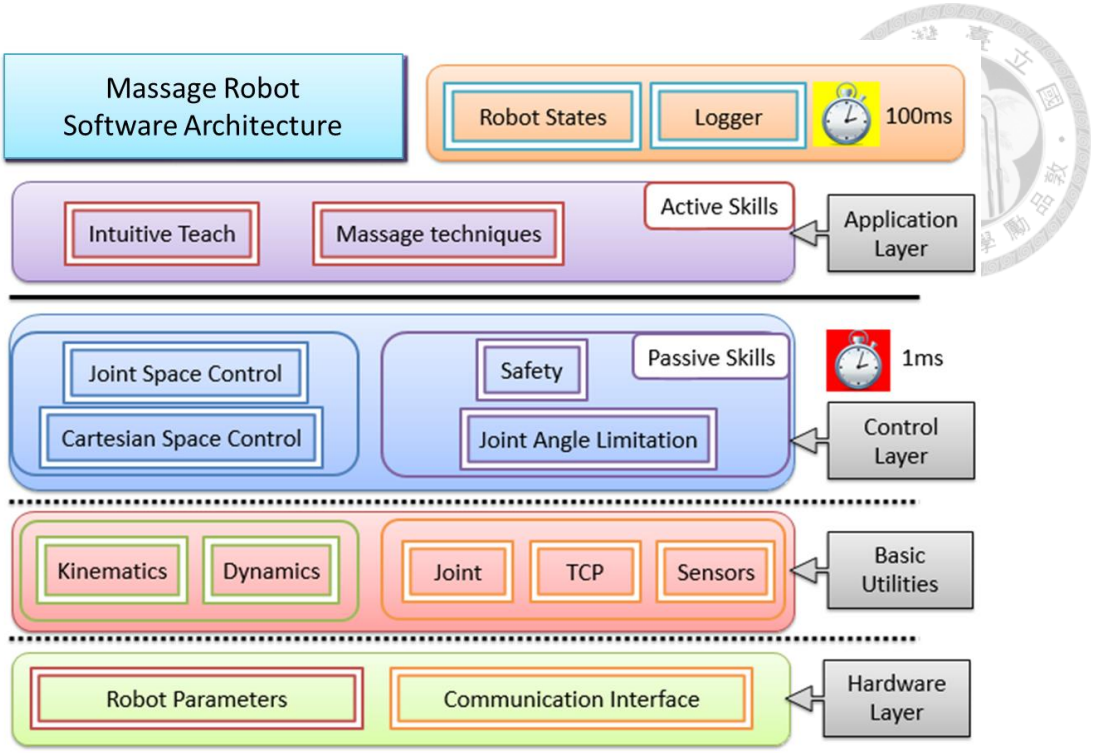

Fig. 2-10 The software architecture of the dual arm robot.

doi:10.6342/NTU201703367

Chapter 3 Control Techniques

In this section, we give an overview of the control techniques applied to robotics massage system. The Cartesian impedance control and joint impedance control which are implemented to achieve the movements of massage are presented first. The impedance control models the external environment as a mass-spring-damper system as shown in Fig. 3-1. Its input is position and output is force. Then the online trajectory generator and gravity compensation of the robot are introduced. Finally, a variety of massage technique are illustrated.

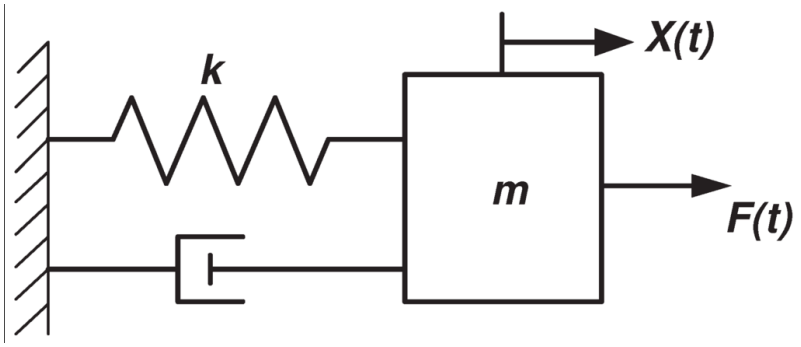

Fig. 3-1 The mass-spring-damper system.

3.1 Cartesian Impedance Control

To ensure safety, we adopt impedance control to implement the massage function and develop different massage techniques based on it.

The manipulator dynamic equation of the robot is given by (3.1).

$$M(q)\ddot{q} + C(q,\ddot{q}) + G(q) = \tau + \tau_{ext} \tag{3.1}$$

where $M(q)$ is inertia matrix of the manipulator, $C(q,\ddot{q})$ is Coriolis and centrifugal matrix, and $G(q)$ represents the gravity term. q is the vector of joint angle. τ and τ_{ext} represent the torque out and the external torque from the environment.

doi:10.6342/NTU201703367

The technique of impedance control [31] considers the external force F_{ext} as a mass-spring-damper system as:

$$F_{ext} = M_e\ddot{\tilde{x}} + D_e\dot{\tilde{x}} + K_e\tilde{x} \tag{3.2}$$

M_e, D_e, and K_e are the matrix of mass, damper and spring of the environment respectively. $\tilde{x}$ represents the displacement of outside environments (Fig. 3-2) as follow:

$$\tilde{x} = x - x_0 \tag{3.3}$$

where x_0 is the equilibrium position and x is the real position encountering the external force.

The relation between the external torque and the external force is shown as (3.4). J is the Jacobian matrix of the manipulator.

$$\tau_{ext} = J^T F_{ext} \tag{3.4}$$

Therefore, the Impedance Control law can be derived as:

$$\begin{aligned}\tau = M(q)J(q)^{-1}\{M_e^{-1}[F_{ext} - D_e\dot{\tilde{x}} - K_e\tilde{x}] - \dot{J}(q)\dot{q}\} \\ +C(q,\ddot{q}) + G(q) - J^T F_{ext}\end{aligned} \tag{3.5}$$

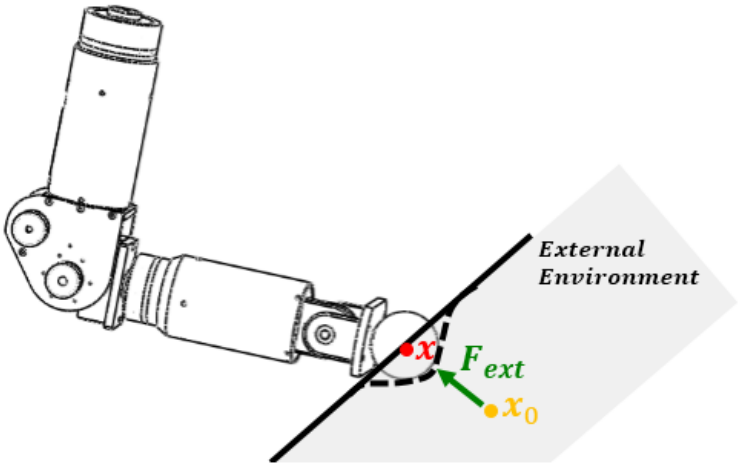

Fig. 3-2 The schematic diagram of manipulator with external environment.

doi:10.6342/NTU201703367

3.2 Joint Impedance Control

Because it is difficult to give the command in Cartesian space for some massage techniques, we also adopt the joint impedance control in the robot system. Joint impedance control [32] can give the command in joint space while keep compliance. It is used to achieve the lead-through capability that users are able to teach the desired trajectory by leading the robot arms themselves.

From the electric and mechanical dynamics of the motor and joint, the basic equations are formulated as follow:

$$L\frac{di}{dt} + RI_e = V - V_b \tag{3.6}$$

$$J_m\ddot{q} + C_m\dot{q} = \tau_{load} - \tau_d \tag{3.7}$$

where L and R are motor inductance and resistance, I and V are current and voltage, J_m and C_m are inertial of system load and viscosity coefficient, V_b and τ_d are back EMF voltage and disturbance torque and τ_{load} is the load torque.

If $R \gg L$ ($\tau = K_m I,\ V_b = K_b\dot{q}$), the load torque τ_{load} can be obtained as:

$$\tau_{load} = J_m\ddot{q} + \left(C_m + \frac{K_m K_b}{R}\right)\dot{q} + \tau_d \tag{3.8}$$

And the impedance control law can be described as:

$$\tau = K_{im}(q_r - q) + D_{im}(\dot{q}_r - \dot{q}) + J_m\ddot{q} + \left(C_m + \frac{K_m K_b}{R}\right)\dot{q} + \tau_d \tag{3.9}$$

where K_{im} and D_{im} are the proportional and derivative impedance gains, and q_r is desired angular position.

3.3 Online Trajectory Generator

Due to the of impedance control, when the desired position is far from the actual position, it will cause a larger output torque which will make the robot out of control an;

doi:10.6342/NTU201703367

on the other hand, when the actual position is very near to the desired position, the output toque will be too small which cause the error between these two position. To conquer this problem, we add the online trajectory generator in the Cartesian impedance control so that the speed of the robot motion can be regulated.

The speed of a trajectory can be divided into three phases including acceleration phase, uniform phase and deceleration phase as shown in Fig. 3-3.

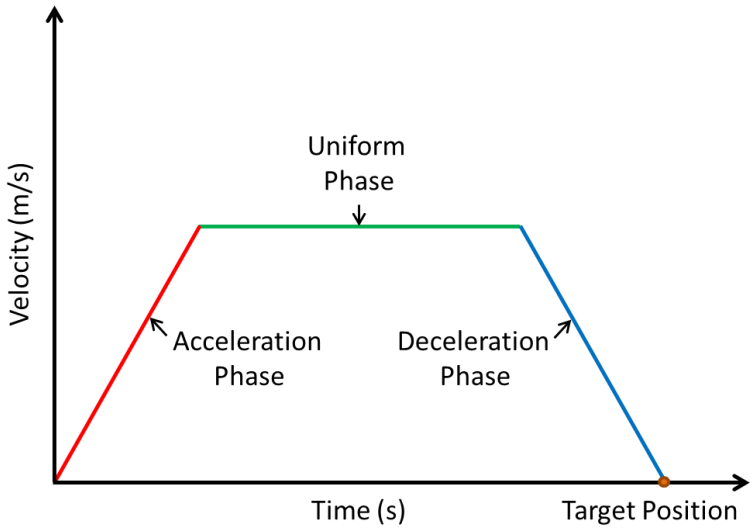

Fig. 3-3 Three phases of online trajectory generator.

In the acceleration phase, the speed of the robot arm is limited to prevent from exceeding the maximum acceleration. It is presented as:

$$if\ \dot{x} > \dot{x}_{t-1} + \ddot{x}_{max}t$$
$$then\ \dot{x}_0 = \dot{x}_{t-1} + \ddot{x}_{max}t \tag{3.10}$$

where $\ddot{x}_{max}$ is the maximum acceleration/deceleration in on-line trajectory generator. $\dot{x}$ is the actual velocity, $\dot{x}_{t-1}$ is the velocity at last sampling time and $\dot{x}_0$ is planned velocity.

doi:10.6342/NTU201703367

In the uniform phase, the arm motion goes with uniform speed. Its speed can be constrained as:

$$if\ \dot{x} > \dot{x}_{max}\ \ then\ \ \dot{x}_0 = \dot{x}_{max} \tag{3.11}$$

Finally, when the actual position is close to desired position, the arm motion enters deceleration phase. It can be presented as:

$$if\ \dot{x} > \sqrt{2\ddot{x}_{max}S}\ \ then\ \ \dot{x}_0 = \sqrt{2\ddot{x}_{max}S} \tag{3.12}$$

Fig. 3-4 shows the control diagram of Cartesian impedance control. The encoder feedback is transformed to the current position, velocity, and acceleration as the input of trajectory generator. Then the planed positon can be obtained with:

$$x_p = x_{t-1} + \frac{1}{2}(\dot{x}_0 + \dot{x}_{t-1})t \tag{3.13}$$

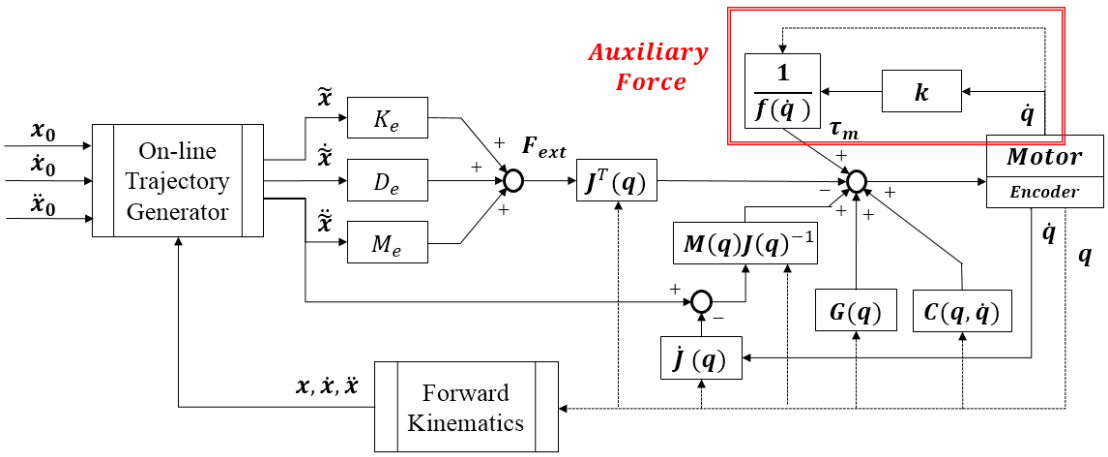

Fig. 3-4 The control diagram of Cartesian impedance control.

doi:10.6342/NTU201703367

3.4 Gravity Compensation

For gravity compensation, the compensation torque is computed by calculating Jacobin matrix in each configuration of the manipulator. The Jacobian transpose is described in (3.14).

$$\tau = J^T F \tag{3.14}$$

From the definition of Jacobian, the velocity in Cartesian coordinate $\dot{x}$ can be presented by the angular velocity in joint space $\dot{q}$ and the Jacobian matrix (3.15).

$$\dot{x}_{6\times1} = \begin{bmatrix} V_{3\times1} \\ \omega_{3\times1} \end{bmatrix} = \begin{bmatrix} J_V(q) \\ J_\omega(q) \end{bmatrix}_{6\times n} \dot{q}_{n\times1} \tag{3.15}$$

where $J_V(q)$ and $J_\omega(q)$ are determined as follow:

$$J_v(q) = P(\dot{q}) \tag{3.16}$$

$$J_\omega = \begin{bmatrix} {}^1R_z & {}^2R_z & \cdots & {}^nR_z \end{bmatrix} \tag{3.17}$$

where ${}^nR_z$ represents the z-axis component in transformation matrix ${}^0_nT$ which is shown as:

$${}^0_nT = \begin{bmatrix} {}^0_nR & {}^0_nP \\ 0 & 1 \end{bmatrix} \tag{3.18}$$

Then the gravity compensation can be achieved by (3.18) and properly defining the center of gravity and mass of each link.

doi:10.6342/NTU201703367

3.5 Massage Techniques

There is a variety of massage techniques realized by our dual arm robot such pressing, rubbing, stroking, and tapping. We will focus on the first 3 techniques in this section.

3.5.1 Pressing

Pressing is a technique to perform the periodical pressing movement on a single point. Its force $F_{pressing}$ is determined by the impedance parameters and the virtual target point x_0. Its function can be expressed as below:

$$F_{pressing}(x_0, t) = F_{ext}(x_0)\Omega(t) \tag{3.19}$$

$F_{ext}(x_0)$ represents the amplitude in periodical movement. $\Omega(t)$ as defined in (3.20) is the sigmoid function that determines the pressing time and the indentation speed. η is the time constant used for waiting the rising and falling edges; T is the pressing time after reaching the desired pressing force from (3.19) and a is the index for the designed sigmoid function.

$$\Omega(t) = \begin{cases} \dfrac{1}{1 + e^{-a\left(t-\frac{\eta}{2}\right)}}, & 0 \le t < \eta \\ 1, & \eta \le t < \eta + T \\ \dfrac{1}{1 + e^{a\left(t-\frac{3\eta}{2}-T\right)}}, & \eta \le t < \eta + T \end{cases} \tag{3.20}$$

3.5.2 Rubbing

Rubbing is the technique that uses palm or thumb to apply pressure maintained on the human skin. It moves by following a circular trajectory to loosen the tight muscles.

doi:10.6342/NTU201703367

The same as pressing, we need to determine the virtual target point for generating proper rubbing force. Its motion can be realized by (3.21).

$$x_0 = \begin{bmatrix} x \\ y \\ z \end{bmatrix} = \begin{bmatrix} rcos\theta \\ \lambda_1(-x + \lambda_2) \\ rsin\theta \end{bmatrix} \quad (3.21)$$

where x_0 is the planed position, r is the radius of circular motion, θ is the incremental angle of rubbing technique and both λ_1 and λ_2 are the coefficients to compensate the slope of human back.

3.5.3 Stroking

Stroking is a long and smooth movement with moderate pressure over large range of the body. Since the profile of the human body is varied from person to person and the stroking technique needs to maintain the moderate contact force along the profile of body, the stroking trajectories are taught by the masseur that intuitively moves the robot arms in order to repeat the motion when performing the stroking technique. Joint impedance control which is presented in 3.2 is used to achieve the stroking technique. The trajectory of stroking will be saved in the storage as a sequential command in joint space.

doi:10.6342/NTU201703367

Chapter 4 Low-Cost Laser Range Finder

There have been researches discussing massage trajectory planning, but they often generate the trajectories through teach and play or user interface. Those are not an automated process and unsuitable for different body shapes. Another stumbling block for massage robots is the sensors which are indispensable to robotics service applications. In order to generate the massage trajectory accurately without other people's help and lower the cost at the same time, we propose an adaptive trajectory generation system by using a self-developed low-cost laser range finder (LRF) that can get the 3D information with a single scan. In this chapter we firstly introduce the hardware and software system of the self-developed laser range finder; then the laser based line scanner module which is applied on the LRF is presented. We prove the performance by comparing the accuracy of the self-developed LRF and the commercial product and scan lots of objects to show its capability as well.

4.1 System Description

Fig. 4-1 shows the structure of the self-developed laser range finder. It has the following specifications.

1) Size of 270[mm]x75[mm]x105[mm]

2) Eye-safe (Class II)

3) Measurable Range: 0.35[m]~4[m] for distance measurement

(0.35[m]~1.75[m] for adaptive trajectory generation)

4) High Resolution: 7.35[mm] range resolution at 1.75[m]

5) Wide Scanning Range: 300[deg] with angular resolution of 0.29[deg]

6) Scanning Time: 400[ms/deg]

doi:10.6342/NTU201703367

7) Extracting 3D information with a single scan

8) Low Cost: less than 70USD to build

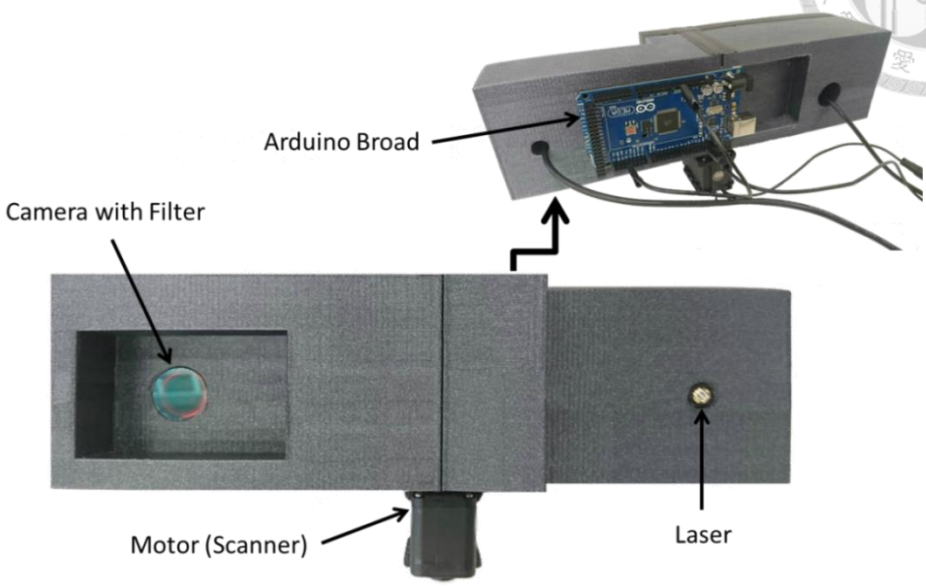

Fig. 4-1 The structure of the self-developed laser range finder.

Fig. 4-2 The components of the self-developed laser range finder.

The laser range finder is composed of a line laser, a commercial camera which communicates with the computer through USB, a Dynamixel AX-12A motor from Robotis for yaw rotation, and an Arduino for motor control and data transmission (Fig. 4-2). The camera and motor is synchronized through software (Fig. 4-3). The time

doi:10.6342/NTU201703367

difference of synchronization is 0.12s. Because the rotation speed of the motor is not fast (400ms/deg), we still can capture corresponding image from camera. It is acceptable in this application. Our LRF system performs on a Windows 7 64bit i5-4460 3.20GHz with 16GB RAM. The total power consumption is about 1.525W. It should work just as well on smaller or mobile platforms like the Raspberry Pi. All components are commercial products bought online. Their prices are shown in Table 4-1. The total price is 69 USD which is less than 10% of the price of the commercial product such as SICK and Hokuyo. Its aggregate price can be much lower after it enters the mass production stage.

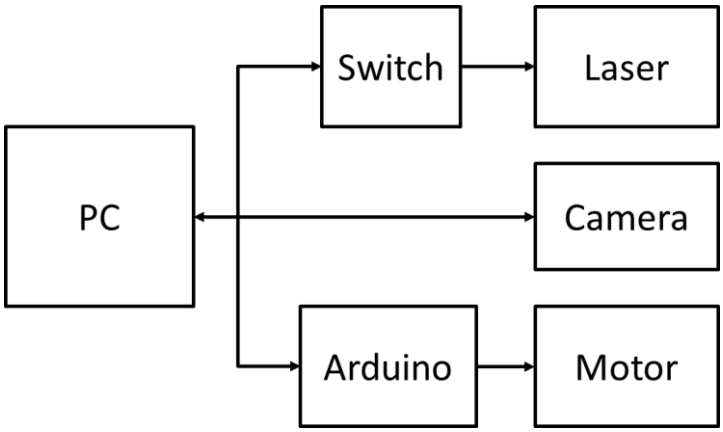

Fig. 4-3 The block diagram of the electronic components.

Component	Product Type	Price (USD)
Line Laser	FU635L5-C9	3
USB Camera + Filter	KINYO PCM-512	16
Motor	Robotis Dynamixel AX-12A	40
Circuit Board	Arduino mega 2560	10
		Total: 69

Table 4-1 The price and the product type of the component.

There is a tradeoff between getting better performance and maintaining safety. To

doi:10.6342/NTU201703367

ensure the eye safety, we should choose the laser which doesn't cause the eyes harm. The power level of laser is divided into 4 classes. Class 1 means it is safe under all conditions of normal use and Class 2 represents the laser damages to the retina can be prevented by the blink reflex (0.25 seconds exposure time). The class above Class 3 will have the high risk of serious damage to eyes. Table 4-2 shows the accessible emission limits for laser systems formulated by ANSI Z136 [33] which provides guidance for the safe use of lasers and laser systems. The wavelength of the line laser is 635nm (visible light) that is easier to debug and calibrate than IR wavelengths, so we pick 1mW for the power of laser which is able to acquire the best results with keeping eyes safe. In the future, we will change the light source to near infrared ray to give the user a more comfortable sensory experience.

Wavelength Range (um)	Emission Duration (s)	Class 1 (W)	Class 2 (W)	Class 3 (W)	Class 4 (W)
Ultraviolet: 0.302~0.4	$3x10^{4}$	$\leq 3.2x10^{-6}$	--	>Class 1 but ≤0.5	>0.5
Visible: 0.4~0.7	10	$\leq 0.4x10^{-3}$	>Class 1 but $\leq 1.0x10^{-3}$	>Class 2 but ≤0.5	>0.5
Near Infrared: 0.7~1.05	≥10	$\leq 0.4x10^{-3}$ to $\leq 1.9x10^{-3}$	--	>Class 1 but ≤0.5	>0.5

Table 4-2 Emission limits for laser systems

In most environments, the received laser is affected by ambient light. There are 3 methods usually used to reject the ambient light as below. The first method is not suitable for outdoor environment because of sun light and the second method cannot

doi:10.6342/NTU201703367

deal with the environment that has the fluorescent lamp. Because of the aforementioned reasons and cost consideration, we select the third one and add a 30nm bandpass filter to reduce the ambient light flux. The camera with filter has capability of not to capture clear images from people for avoiding privacy issues.

1) Adjusting the exposure time of camera

2) Using IR light as laser source

3) Adding Filter

4.2 Laser Based Line Scanner Module

Laser based line scanner module is developed from laser point sensor module [18] which is based on triangulation technology. Most of commercial products such as SICK and Hokuyo devices use time-of-flight (TOF) technology. They measure the time it takes for light to travel to an object and be reflected. The disadvantage of time-of-flight is that its receiver is very expensive and it often takes mirror as scanner of which cost and mechanical fragility are high. An alternative technology is triangulation. Its principle is that the distance to an object is measured by the angle of the reflected light and we can replace mirror with motor as scanner to cost down.

Fig. 4-4 shows the triangulation geometry of single-point laser sensor module. A laser produces a small point of light, which reflects off an object and onto the image plane of the camera. To give an ideal distance measurement from infinity, the laser beam needs to be parallel to the ray through the center of focus to the one edge of the image. The other edge of the image determines the minimum distance q_{min}.

The perpendicular distance D to the target according to basic triangulation principle can be calculated as follow:

doi:10.6342/NTU201703367

$$D = \frac{fL}{x} \tag{4.1}$$

where f is the focal length of the camera, L is the distance between the laser and the center of image lens also called baseline, and x is distance between the edge of image and the position where the reflected laser point intersects the image plane.

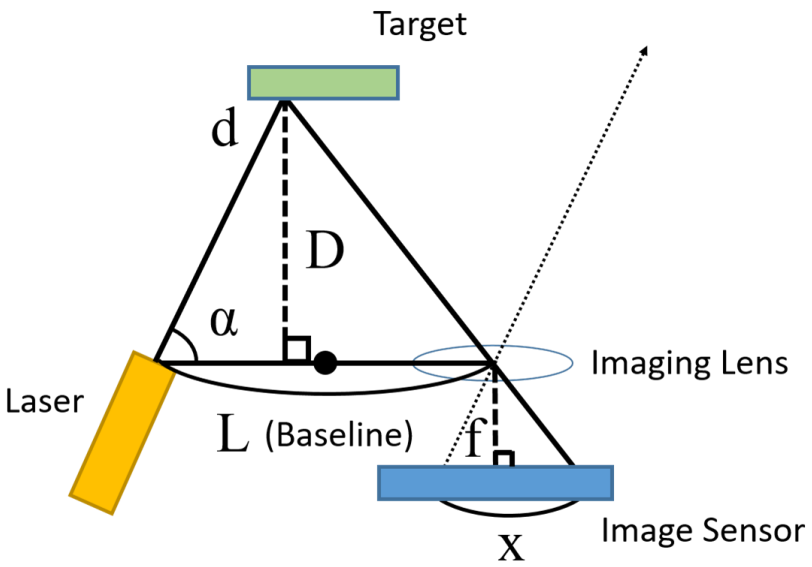

Fig. 4-4 Triangulation geometry of single-point laser sensor module.

The distance d along the laser ray which depends on the angle of the laser α with respect to the image axis can be derived from D as (4.2).

$$d = \frac{D}{sin(\alpha)} \tag{4.2}$$

These two equations figure out the hyperbolic relationship between image distance and object distance which is a property of triangulation. This nonlinear relationship has the problems for determining longer distances. That is, the range sensitivity $\frac{dD}{dx}$ grows quadratically with distance as (4.3).

$$\frac{dD}{dx} = -\frac{D^2}{fL} \tag{4.3}$$

doi:10.6342/NTU201703367

For example, if a 1-pixel image displacement corresponds to a 1 cm distance displacement at 1m, then it corresponds to a 4 cm displacement at 2 m.

Although basic triangulation technology is easy to implement, it only can get 2D information with one scan which does not meet our requirement. Therefore, we adopt laser based line scanner module [34] that is developed from laser point sensor module.

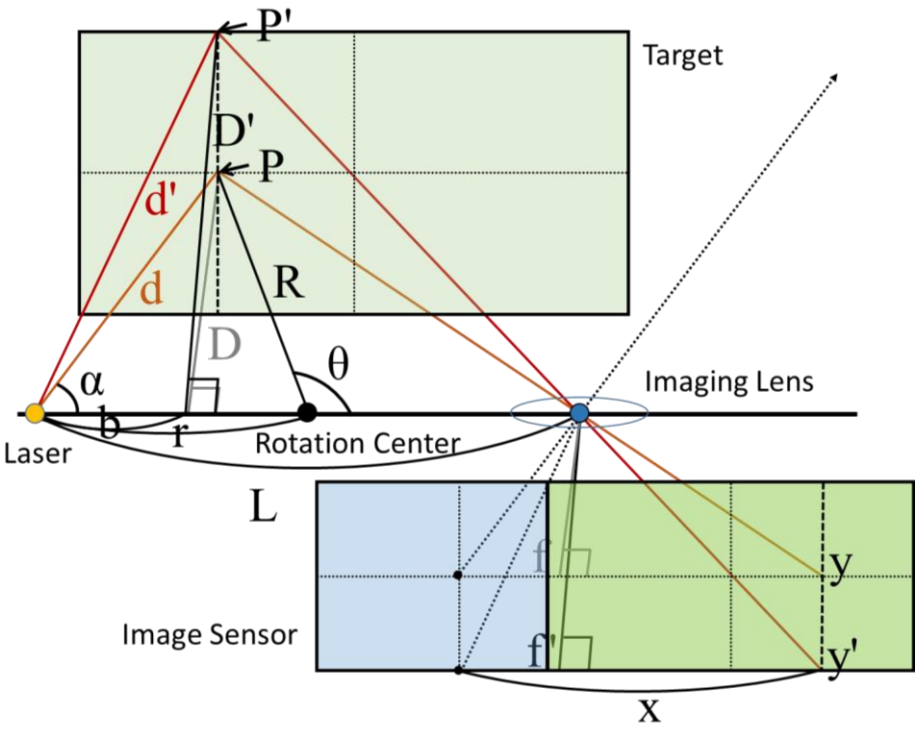

Fig. 4-5 Triangulation geometry of laser based line scanner module.

Fig. 4-5 shows the triangulation geometry of laser based line scanner module. We can consider the line laser as many point lasers with different tilt angle in set P_n where n is the number of laser points. When the laser point hits the center of the target without any tilt angle as point P to make its reflected light intersect the imaging plane at y which is in the middle of the image sensor, we can calculate the perpendicular distance D to the target as (4.1).

If the laser has a tilt angle and hits the target as point P', the reflected light and the imaging plane will intersect at y'. For this condition, we cannot use the original focal

doi:10.6342/NTU201703367

length f to calculate the perpendicular distance. The adjusted perpendicular distance D' is able to be obtained with:

$$D' = \frac{f'L}{x} \tag{4.4}$$

where the modified focal length f' can be derived from the triangulation geometry as shown in (4.5).

$$f' = \frac{f}{cos(arctan(\frac{y' - y}{f}))} \tag{4.5}$$

For trajectory planning, we need to know the distance R_n between the rotation center and the target laser point (P_n) and the angles θ and ϕ as shown in Fig. 4-6 to find the spatial relationship between the robot and the target. The distance r from the laser center to the rotation center is one-half the length of the baseline as 100mm. We can calculate the distance R_n and the angles θ and ϕ by the following equations:

$$R_n = \sqrt{(r-b)^2 + D_n^2} \tag{4.6}$$

where b is the distance between the laser center and the projection of the point P_n on the baseline.

$$\theta = \begin{cases} \pi - arcsin\left(\frac{D}{R}\right), & if\ b \le r \\ arcsin\left(\frac{D}{R}\right), & otherwise \end{cases} \tag{4.7}$$

$$\phi = \begin{cases} arccos\left(\frac{R}{R_n}\right), & for\ upper\ half-plane \\ -arccos\left(\frac{R}{R_n}\right), & for\ lower\ half-plane \end{cases} \tag{4.8}$$

doi:10.6342/NTU201703367

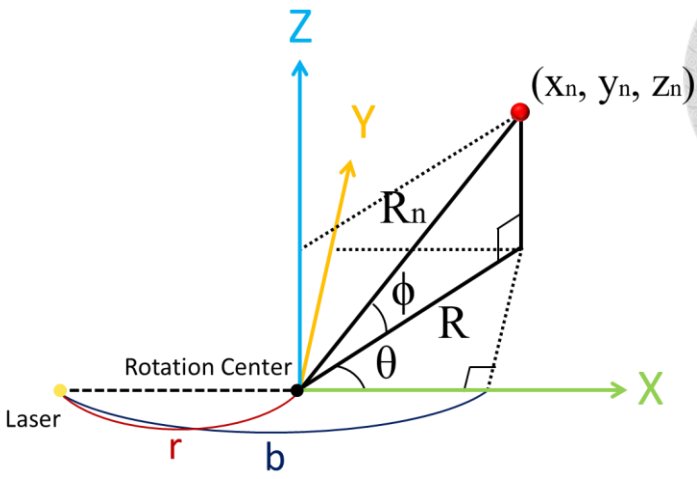

Fig. 4-6 The spatial relationship between the laser dot and the rotation center.

After we get the R_n, θ, and ϕ, the position of the laser dot according to the frame of the laser range finder can be obtained with:

$$\begin{cases} x_n = R \times cos(\theta) \\ y_n = R \times sin(\theta) \\ z_n = R_n \times sin(\phi) \end{cases} \tag{4.9}$$

To achieve more accurate results, we adopt the centroid algorithm provided by [18] for localization to make the laser dot be localized to subpixel precision. The centroid of the laser dot at each row can be calculated by:

$$\sum_i I(i) \cdot i / \sum_i I(i) \tag{4.10}$$

where i means the position of each pixel at the row and $I(i)$ is the intensity or pixel value of i.

Then we can determine the parameters of laser based line scanner module to satisfy our requirements. The focal length f of the camera we use is 6.25mm and we expect to be able to resolve the laser dot to within 0.5 pixel. The criteria for minimum distance and range resolution pull in opposite directions due to hyperbolic relationship: a small fL product gives a small q_{min}, a large fL has good range resolution. We choose

doi:10.6342/NTU201703367

baseline L as 200mm to get the product $fL = 1250$ so that the minimum distance is 32.5cm and the range resolution is 7.35mm with 0.5 subpixel accuracy at 1.75m which meet our needs.

The angle α is determined by the intrinsic parameters and the optical axis which is obtained as follow:

$$\alpha = arctan(\frac{f}{\frac{width\ of\ image}{2} * pixel\ size}) \tag{4.11}$$

The resolution of the camera we use is 640*480 pixels and each pixel is 6um, so the angle α is:

$$\alpha = arctan(\frac{6.25mm}{\frac{640}{2} * 6um}) \approx 73^{\circ}$$

4.3 Performance and Comparisons

We validate the module by comparing its accuracy with the Hokuyo URG-04LX laser range finder [35] (Fig. 4-7) on the white target with 90% reflectance. The Hokuyo LRF is mounted on the center of the self-developed LRF to make sure they have the same datum and we use the Hokuyo laser range finder as ground truth and find the difference between our laser range measurements and the Hokuyo. The measured range is from 35cm to 4m.

Fig. 4-7 Hokuyo URG-04LX laser range finder.

doi:10.6342/NTU201703367

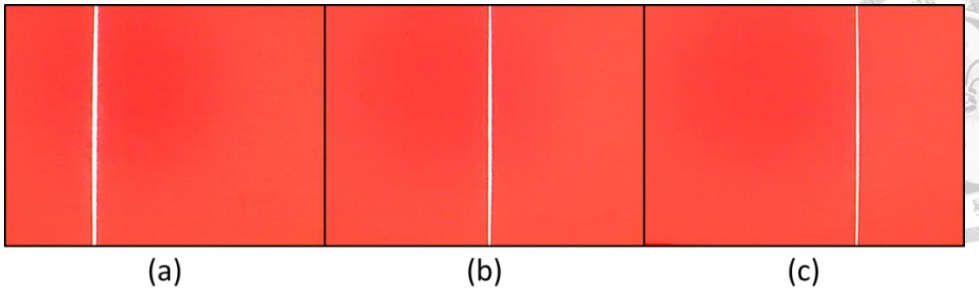

Fig. 4-8 The images captured from the camera at difference distance. (a) 0.45m (b) 0.65m (c) 0.9m

Fig. 4-8 shows the images captured from the camera at difference distance. We can apparently find that the shorter the distance, the smaller the interval between the laser line and the left edge of the image. That means the shorter distance has the larger x in (4.4), which conforms to the principle of triangulation.

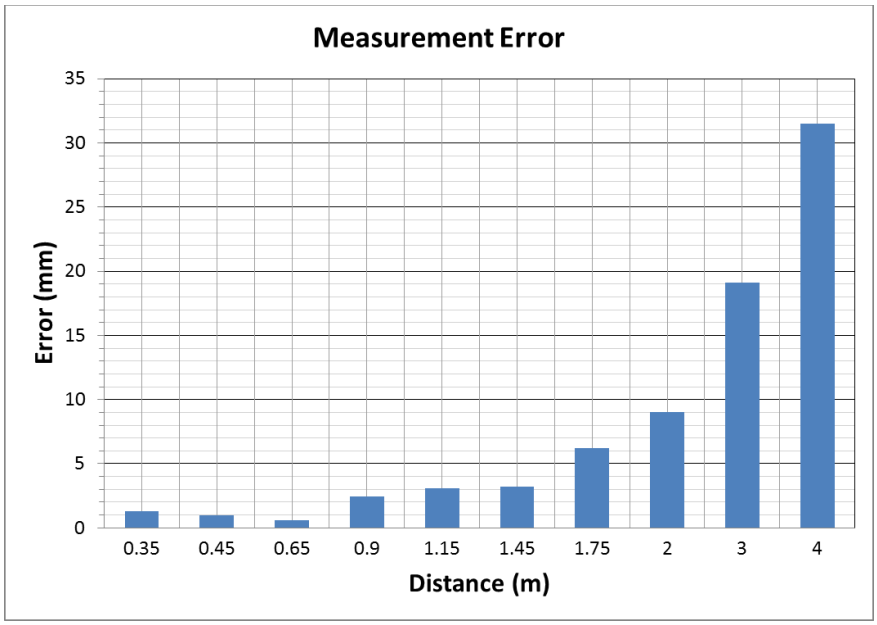

Fig. 4-9 Distance errors for 90% reflectance.

The errors are shown in Fig. 4-9. The farther distance has the larger error with a lower range resolution due to the nonlinear relationship ($dD/dx = -D^2/fL$) of triangulation. The errors are within 3mm at a range of up to 0.9m and the error is 6.21mm at 1.75m. Since there are more pixels becoming saturated at closer distances,

doi:10.6342/NTU201703367

the errors at 0.35m and 0.45m are higher than the error at 0.65m. All error rates are below 0.75% which means the module has comparable performance as the commercial product.

We also test it by constructing the 3D surface of a box in Fig. 4-10. The objects are put in front of the LRF 1m away. The widths of the box are 15cm (shorter side) and 20cm (longer side) respectively and it height is 20cm. The diameter of the teapot's bottom is 15cm and the height is 22cm. The scanning result is very similar to the real object and the scale of the box is reproduced accurately although the area around the blue circle is influenced by the blue color which reduces the intensity of reflected light. Despite this, the laser module works very well.

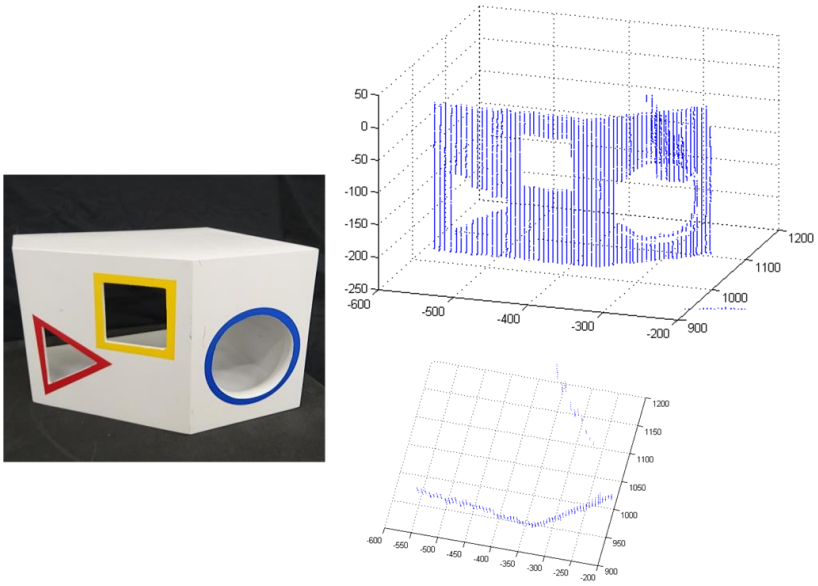

Fig. 4-10 We test the module by constructing the 3D surface of a box. Here presents the result in front view and top view.

Here presents some other scanning results to reverify the performance of the self-developed LRF (Fig. 4-11). The tested objects from the left side to the right and from top to bottom are teapot, ukulele, NAO (a robot made by Aldebaran), basketball, jenga, and shoe.

doi:10.6342/NTU201703367

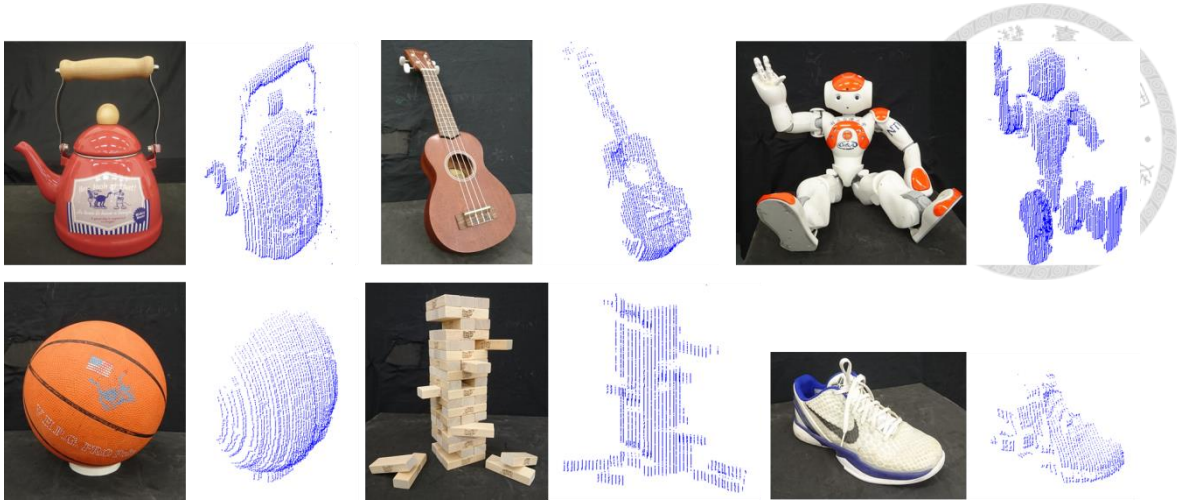

Fig. 4-11 Scanning results of different objects.

doi:10.6342/NTU201703367

Chapter 5 Adaptive Trajectory Generation

The adaptive trajectory generation system we propose can completely automate the trajectory planning procedure and generate the adaptive and precise trajectories for different people. Our method is based on the morphing algorithm [36]. We first construct the standard 3D model which indicates the acupressure points of general human back, and then extract the back contours of the standard 3D model and subject by human back feature extraction. After we get the contour, we can map the standard 3D model on the back of the subject using the morphing algorithm to find the acupressure points and generate the adaptive trajectories. Fig. 5-1 is the flow chart.

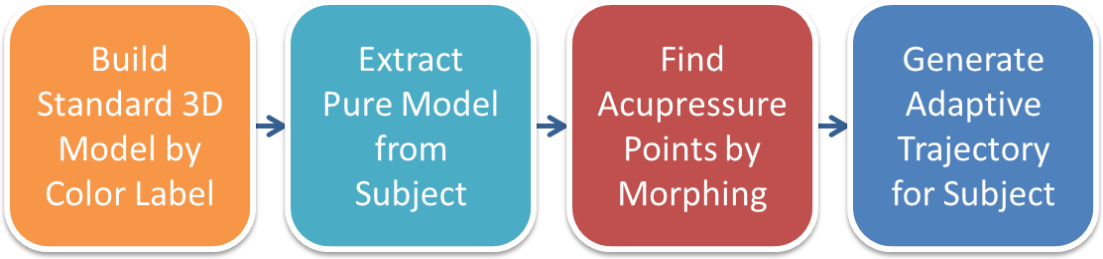

Fig. 5-1 The flow chart of adaptive trajectory generation.

5.1 Standard 3D Model Building

Acupressure Point	Functions
46-Tianzong	Shoulder Pain, Arm Pain, Facial Pain, and Anxiety
47-Humen	Back Pain, Hypochondrium Pain, and Insomnia
49-Weicang	Back Pain, Bloating, and Digestive Disorders
71-Mingmen	Backache, Tiredness, Dizziness, and Tinnitus

Table 5-1 Functions of each acupressure point.

The standard 3D model is developed from one person with medium build. We adopt 7 acupressure points on the human back as shown in Fig. 5-2(Left) which are

doi:10.6342/NTU201703367

usually used to alleviate pain in Chinese medical applications [37] and their functions are presented in Table 5-1. Then we mark these points with color labels on a human back as shown in Fig. 5-2(Right).When the laser hits on the labels, we can get the position of the laser dots with Algorithm 1 and know the position of acupressure points in 3D space. Fig. 5-3 shows the standard 3D model where the acupressure points are marked red.

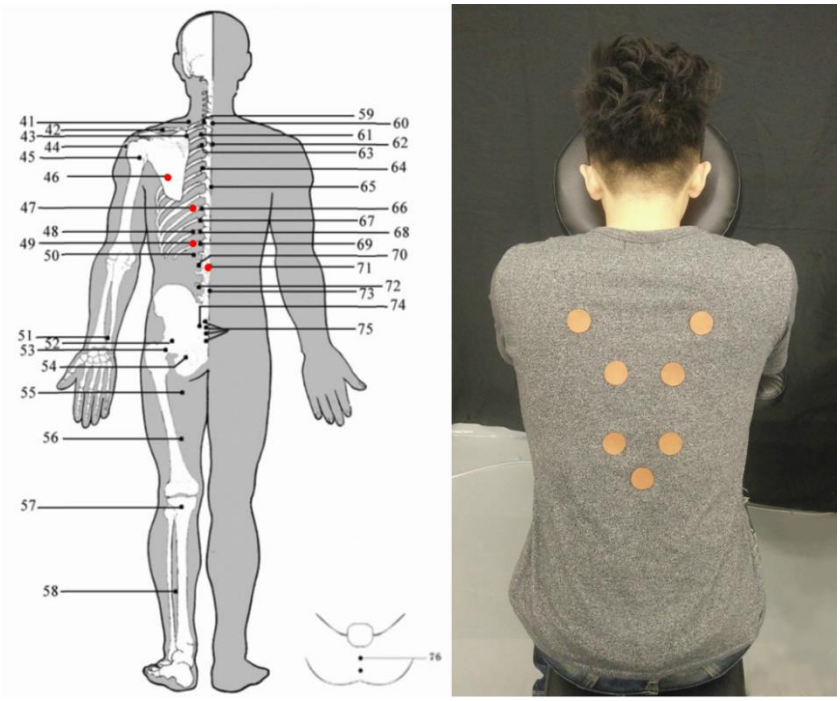

Fig. 5-2 Left: 7 acupressure points on back. Right: We mark them by color labels.

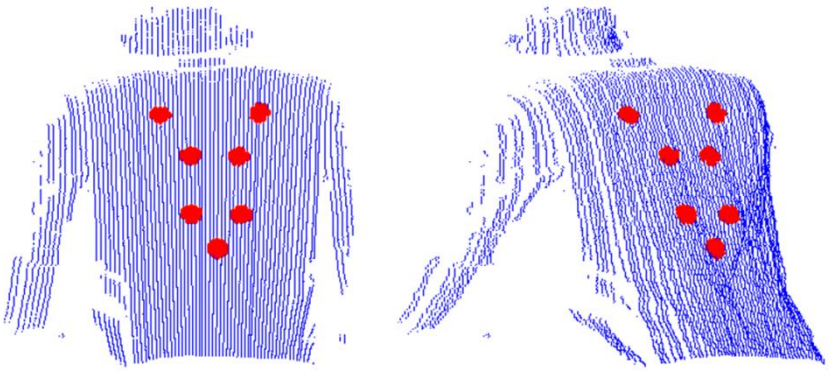

Fig. 5-3 The standard 3D model which indicates the acupressure points on back.

doi:10.6342/NTU201703367

Algorithm 1: Acupressure Points Localization

Input: A captured image with n pixels $[P_0, \ldots, P_{n-1}]$
Output: A image with n pixels $[X_0, \ldots, X_{n-1}]$
displaying the laser dots on the labels

```
for i = 0; i < n; i++ do
    if pixel value of P_i ≥ threshold of laser dot then
        set P_i as laser dot;
    else if pixel value of P_i ≥ threshold of label then
        set P_i as label dot;
    else
        set P_i as background;
    if P_i is a laser dot surrounded by label dots then
        pixel value of X_i = 255;
    else
        pixel value of X_i = 0;
```

5.2 Morphing Algorithm

Fig. 5-4 The processing of morphing. From the left side to the right are the first image, middle image, and second image.

Morphing is the smooth transformation of one image into another. It has been used as a computer graphics technique for a long time. It effect is presented in Fig. 5-4. As the metamorphosis proceeds, the first image is gradually distorted and is faded out, while the second image starts out totally distorted toward the first and is faded in. The middle image of the sequence is the average of the first source image distorted halfway toward the second one and the second source image distorted halfway back toward the

doi:10.6342/NTU201703367

first one.

Morphing consists of two steps; warping and cross-dissolving. Warping means to distort one image into another to make them have same shape and cross-dissolving is to do the color interpolation of two images.

Since we want to transform the shape of standard model into the shape of subject's back, we will focus on the warping step. There are two methods to warp the images, one is mesh warping which uses point-to-point correspondence and another is field warping that uses line-to-line correspondence instead. Our work is based on the latter one which is provided by [36] because the prior method has too many limits and cannot get the desired result we require. Its approach is described as below.

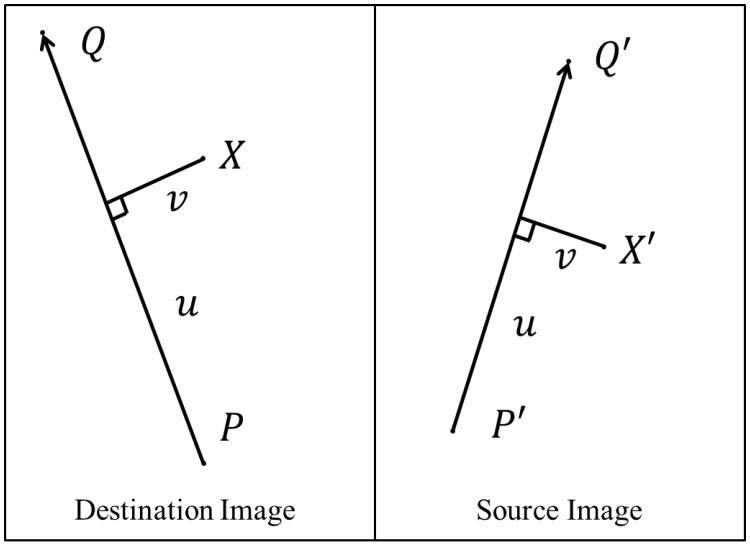

Fig. 5-5 A pair of lines for field morphing.

There is a feature line $P'Q'$ belongs to the source image and a feature line PQ belongs to the destination image as shown in Fig. 5-5. X is the destination image pixel coordinate and we need to find the corresponding pixel coordinate X' in source image and assign its pixel value to X for warping the source image into the destination image that is also called forward mapping. We can get X' by calculating the value u which

doi:10.6342/NTU201703367

means the projection of X on the line and the value v which is the distance from X to the line with following equations:

$$u = \frac{(X - P) \cdot (Q - P)}{\|Q - P\|^2} \tag{5.1}$$

$$v = \frac{(X - P) \cdot Perpendicular(Q - P)}{\|Q - P\|} \tag{5.2}$$

$$X' = P' + u \cdot (Q' - P') + \frac{v \cdot Perpendicular(Q' - P')}{\|Q' - P'\|} \tag{5.3}$$

where $Perpendicular()$ is the vector perpendicular to the vector of ().

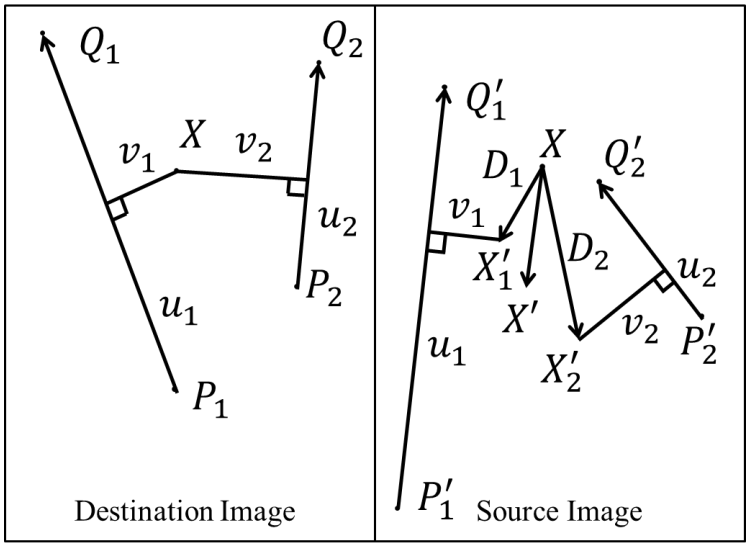

Fig. 5-6 Multiple line pairs for field morphing.

If there are multiple pairs of lines (Fig. 5-6), those specify more complex transformations. The multiple lines algorithm is show in Algorithm 2. The position of X' is influenced by each pair of lines. D_i is the displacement between X'_i in the source image and X_i in the destination image. Then we calculate the weight of each line in the destination image which determines the influence of each pair of lines. The function is written as :

doi:10.6342/NTU201703367

$$weight[i] = \left(\frac{length[i]^p}{(a + dist[i])}\right)^b \tag{5.4}$$

where $length$ is the length of a line. $dist$ is the distance from the pixel to the line, and a, b, and p are constants that can be used to change the relative effect of the lines. The larger a has the smoother warp. The variable b determines how the relative strength of different lines falls off with distance. If p is zero, then all lines have the same weight. If p is one, then longer lines have a greater relative weight than shorter lines. Because these lines are line segments, the line from a point has three conditions as follow:

$$\begin{cases} |v|, & if\ 0 < u < 1 \\ P, & if\ u < 0 \\ Q, & if\ u > 1 \end{cases} \tag{5.5}$$

Algorithm 2: Multiple Lines Algorithm

for *each pixel* X *in the destination* **do**
  $DSUM = (0, 0)$;
  $weightsum = 0$;
  for *each line* P_iQ_i **do**
    calculate u,v based on P_iQ_i;
    calculate X'_i based on u,v and P_iQ_i;
    calculate displacement $D_i = X'_i - X_i$ for line;
    $dist$ = shortest distance from X to P_iQ_i;
    $weight = (length^p/(a + dist))^b$;
    $DSUM+ = D_i * weight$;
    $weightsum+ = weight$;
  $X' = X + DSUM/weightsum$;
  destinationImage(X) = sourceImage(x');

Since we want to map the standard model on someone's back rather than transform it exactly, we adjust the original cross-dissolving equation as (5.6). α is the morphing ratio. If $\alpha = 0$, the shape of the morphing image will be the same as the shape of source image and the pixel values I of the morphing image will equal to the corresponding

doi:10.6342/NTU201703367

warped destination image pixel $I_{destination}$; on the other hand, if $\alpha = 1$, the shape of the morphing image will be the same as the destination image and the pixel values I of the morphing image will be equal to the corresponding warped source image pixel I_{source}.

$$I = (1 - \alpha) * I_{destination} + \alpha * I_{source} \quad (5.6)$$

5.3 Human Back Feature Extraction

To implement the morphing algorithm on a human body model, we project all data on the 2D plane and set a threshold to retain the data of only the back. The 2D plane is determined by the inclined plane of the massage chair. We put a flat plane on a massage chair and scan the plane to get its 3D data. Then we take 3 points on that plane to determine the 2D plane which the models are projected on. The 2D plane is changed according to different method of massage. The result of the standard model is shown in Fig. 5-8(a), and Fig. 5-8(b) is the result of the subject's back.

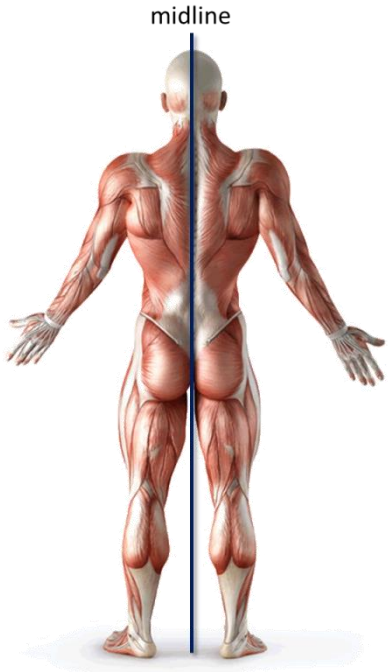

Fig. 5-7 The midline of human body.

doi:10.6342/NTU201703367

We can find the position of the shoulders with simple image processing. We define a midline (Fig. 5-7) (orange line) that is perpendicular and intersects the midpoint of the line (blue line) that connects one shoulder to the other. After we get the midline which divides the body into two halves, we use the endpoints of both lines to estimate the area of the upper back and mark the feature lines (green lines) that describe the shape of back for adaptive trajectory generation.

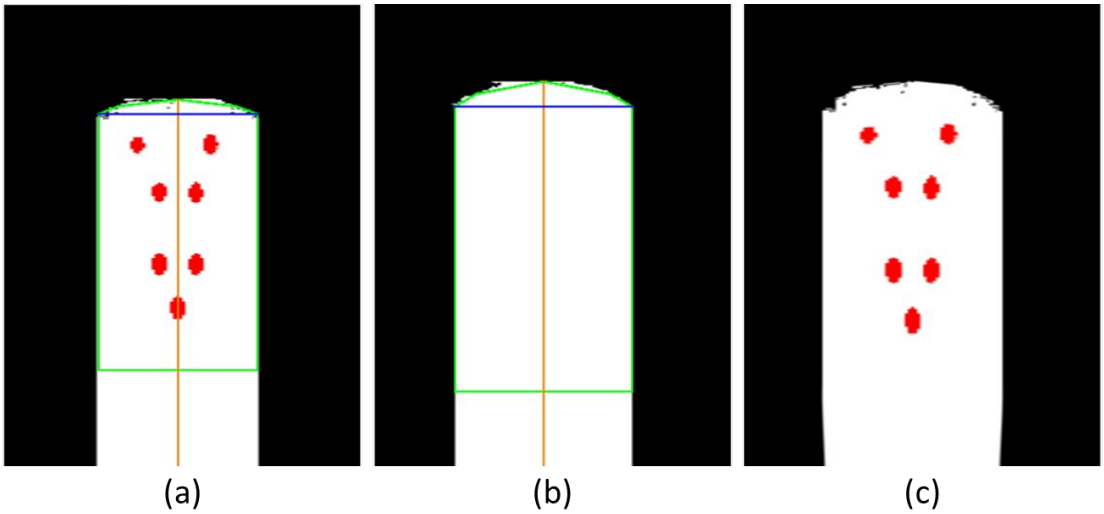

Fig. 5-8 (a) 2D projection of the standard 3D model. (b) 2D projection of the back of subject #1. (c) The result of morphing indicating the acupressure points of subject #1.

5.4 Adaptive Trajectory Generation

Fig. 5-8(c) shows the result of morphing and the average time it takes is 20s. The acupressure points from the standard model are mapped on the back of the subject. To generate the adaptive trajectory, we need to find the position of the acupressure points of the subject's back in 2D space and transform them back into 3D space.

The location of the acupressure points of the subject's back in 3D space can be calculated by following equations:

doi:10.6342/NTU201703367

$$(x_i, y_i, z_i) = \underset{(x_i, y_i, z_i)}{arg\,min} \sqrt{(x_i - X)^2 + (y_i - Y)^2 + (z_i - Z)^2} \tag{5.7}$$

$$(X, Y, Z) = (\sum_{n=1}^{k} \frac{x_n}{k}, \sum_{n=1}^{k} \frac{y_n}{k}, \sum_{n=1}^{k} \frac{z_n}{k})$$

where (x_i, y_i, z_i) is the position of i-th acupressure point (i from 1 to 7) and k is the number of candidates, which are marked as red in morphing image, for i-th acupressure point. We calculate the average position of these candidates and found the closest candidate point as the acupressure point.

5.5 Experimental Results

To verify our proposed method, we try to find the acupressure points of the different subjects with different sizes and compare their results with the real acupressure points which are defined by a massage therapist in advance. The method for determining the real acupressure points is that the massage therapist first recognizes the acupressure points of each subject; and then we use the color labels to mark these points and get the real acupressure points through Algorithm 1 as mentioned before. We put the laser range finder in front of the massage chair 1m away and ask the subject to sit upright in the massage chair for scanning. There are ten subjects in our experiments. Fig. 5-9 shows the 3D model of the hefty subject and the slim subject respectively. The green dots on their backs indicate the real acupressure points and the red dots are the mapped acupressure points from the method we propose. We find that the mapped points are affixed to the surface accurately and the results are very close to the real ones. The average distance error of the acupressure points from ten subjects is 10.7mm that is smaller than the contact radius (17mm) of the sphere-shaped end-effector and the standard deviation of these errors is 2.02mm which means our algorithm can cover all

doi:10.6342/NTU201703367

acupressure points. The root mean square error of the position and the average distance error of the acupressure points for three body types are displayed in Table 5-2. We observe that larger people have bigger errors because their body shape is much more different with average sized people and we should give more features in morphing step to get better fitting. Since the subjects cannot sit exactly upright in the massage chair, it will have a slight rotation along z-axis and yield more significant deviations on the x-axis than y-axis. The experimental results prove our method can precisely generate adaptive trajectory for different people and can be applied in practical applications.

Besides the acupressure points for pressing, we generate the other trajectories for rubbing and stroking through the 6 points as shown in Fig. 5-10 and Fig. 5-11. The radius of rubbing is 3cm and its trajectories are indicated as yellow lines. The trajectories for stroking as magenta lines are planned from the upper points to the lower points and these paths have many acupressure points which are good for our health.

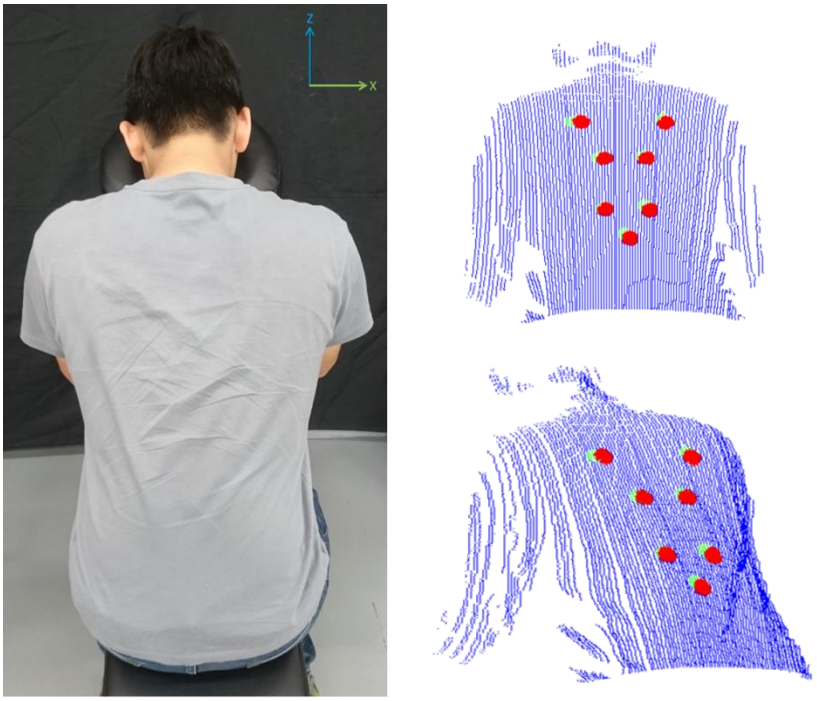

(a) Hefty Subject (Subject #1)

doi:10.6342/NTU201703367

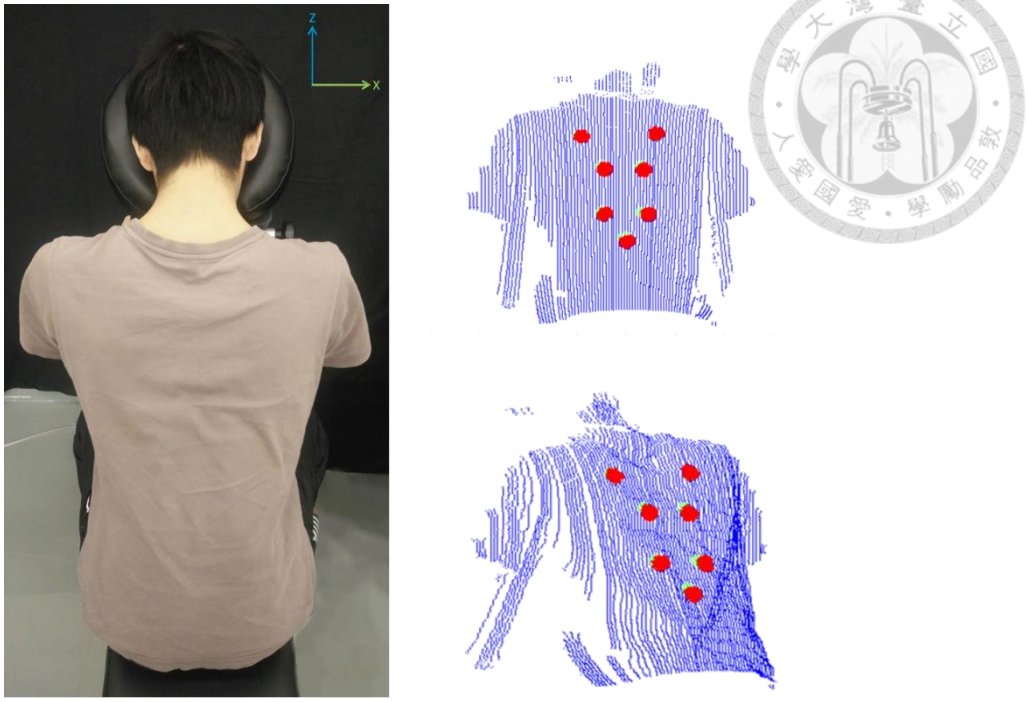

(b) Slim Subject (Subject #3)

Fig. 5-9 The 3D model of the subjects with different body shape. The green dots on their backs indicate the real acupressure points and the red dots are the mapped acupressure points from the method we propose.

Subject	Body Type	BMI	Root Mean Square Error (mm)			Average Error (mm)	Maximum Error (mm)
			x	y	z	distance	distance
Subject 1	Hefty	26	12.4320	3.2190	6.4644	13.8776	14.5952
Subject 2	Medium	21	8.0099	3.8522	5.6659	10.1389	13.9540
Subject 3	Slim	18	8.0000	3.5439	4.8323	9.1740	10.3466

Table 5-2 Errors of trajectory generation

doi:10.6342/NTU201703367

We also record the time that our method takes. The average consuming time of teach and play is more than 75s and the consuming time of our method is 35s. It figures out our method can save more than half the time needed with teach and play.

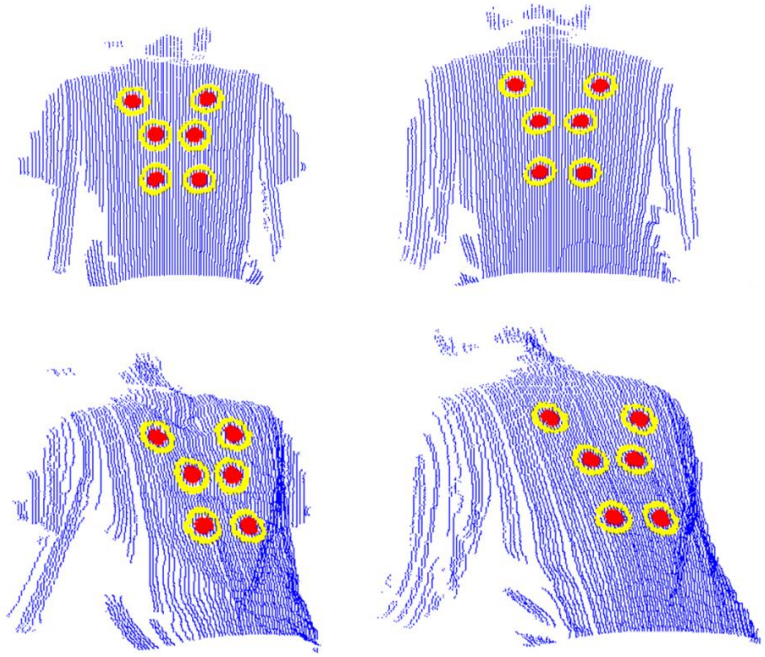

Fig. 5-10 The rubbing trajectories for different subjects.

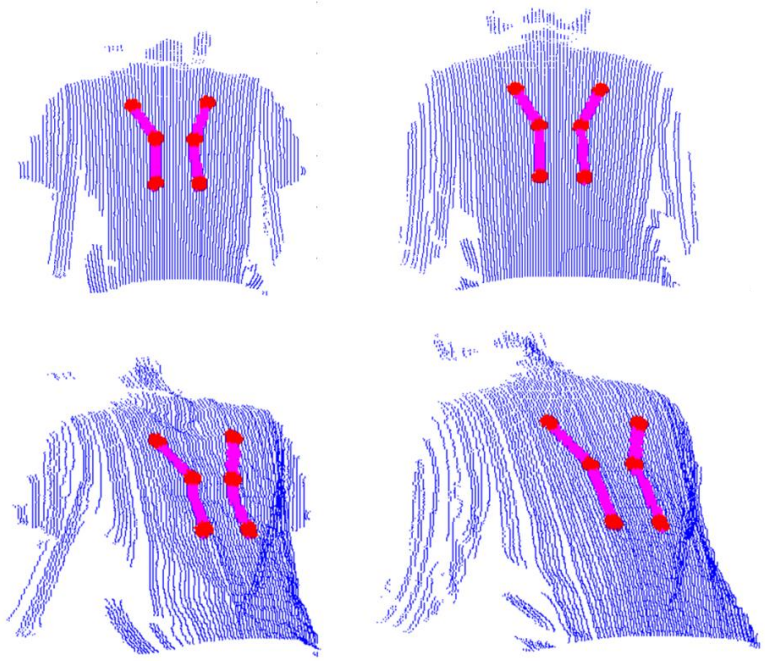

Fig. 5-11 The stroking trajectories for different subjects.

doi:10.6342/NTU201703367

Compare to our previous work [16] as shown in Fig. 5-12. We can apparently find that the trajectories generating from our previous work are very tortuous which are difficult to be applied to practical applications. If the end-effector exactly follows these trajectories, there will be control problems and it will also affect the effectiveness of massage. Because our previous work only use two planes as features for trajectory planning, the trajectories have large offset which are not corresponding to the real trajectories used in general therapeutic massage.

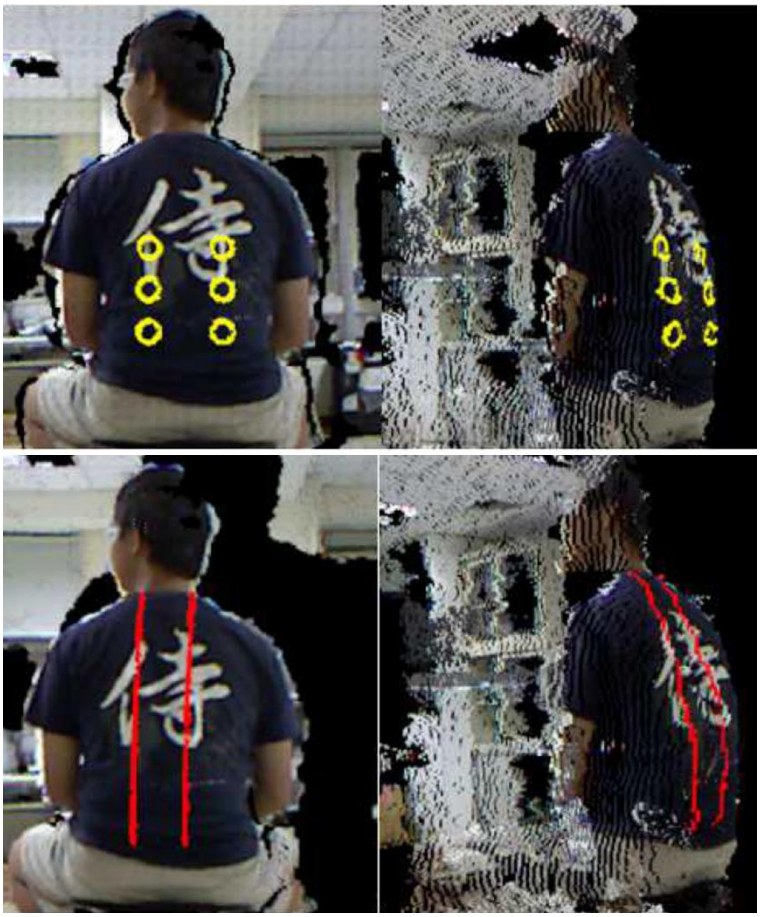

Fig. 5-12 The trajectories generating from our previous work.

In contrast to the previous work, the trajectories from the method in this paper have higher accuracy and are more flat. Furthermore, the acupressure points in this paper are certified by physician that our previous work does not have.

doi:10.6342/NTU201703367

Finally, we apply the self-developed LRF and the adaptive trajectory generation algorithm to the dual robot for massage. There are two scenarios. One is upper body massage that the subject sits upright in the massage chair during massage. Another is full body massage that the subject lies in the massage bed during massage. The dual robot determines the position of acupressure points according to the results of scanning. The relation between the coordinate of the LRF and the coordinate of the dual arm robot is found by camera calibration. The translation is measured by tape measure and the orientation is calculated through the intrinsic parameters and extrinsic parameters of camera. Fig. 5-13 shows the process of the upper body massage.

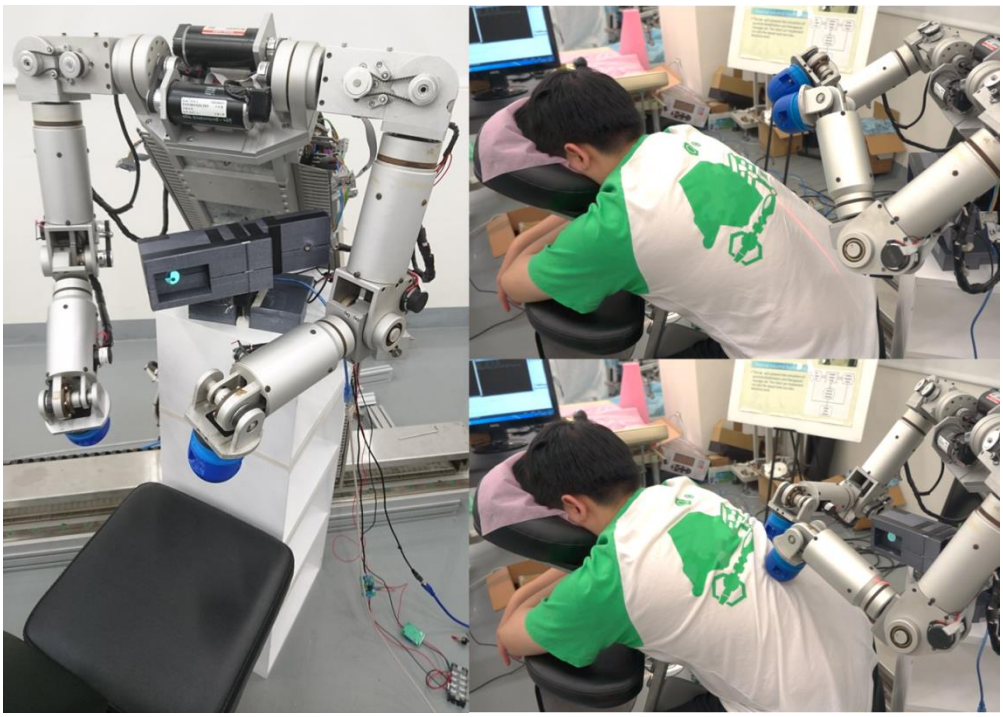

Fig. 5-13 Apply self-developed LRF to upper body massage. Left: The LRF is mounted in front of the dual arm robot. Upper Right: The LRF is scanning the subject's back. Lower Right: The dual arm robot executes pressing on subject's back.

Because each standard model in our algorithm is suitable for only one pose, we rebuild the 3D model for full body massage as shown in Fig. 5-14. In order to be closer

doi:10.6342/NTU201703367

to the real situation, the subject is asked to be bare to the waist. Fig. 5-15 shows the process of the full body massage.

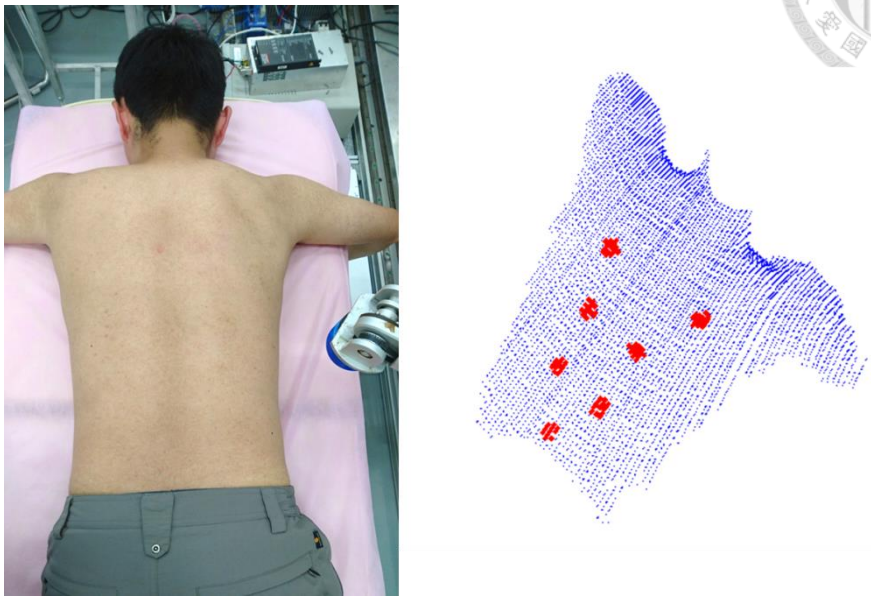

Fig. 5-14 The 3D model of the subject lying on the massage bed.

Fig. 5-15 Apply self-developed LRF to full body massage. Left: The LRF is mounted with a tilt angle in front of the massage bed. Upper Right: The LRF is scanning the subject's back. Lower Right: The dual arm robot executes pressing on subject's back.

doi:10.6342/NTU201703367

Chapter 6 In-Situ Tissue Stiffness Estimation

The main issue of physical human-robot interaction in robotics massage is how to adjust the control strategies according to tissue stiffness to provide patients more comfortable and friendlier service. In this chapter, we first figure out the characteristics of soft tissue by using a 7 DoF robot arm and build an intuitive soft tissue model which have the information of hardness and thickness. Then we present an in-situ tissue stiffness estimation method which can estimate the characteristics of patient's soft tissue during massage. The algorithm is based on adaptive law introduced in this chapter as well and it is verified through simulation and experiment.

6.1 Modeling of Soft Tissue

The soft tissue of the human body contains several layers [38] as shown in Fig. 6-1 including ectodermal tissue, muscles, bones, vessels, etc. Then we can expect that the characteristic of soft tissue should be nonhomogeneous. Before the in-situ tissue stiffness estimation, we need to figure out the characteristic of the soft tissue and to get its approximate model.

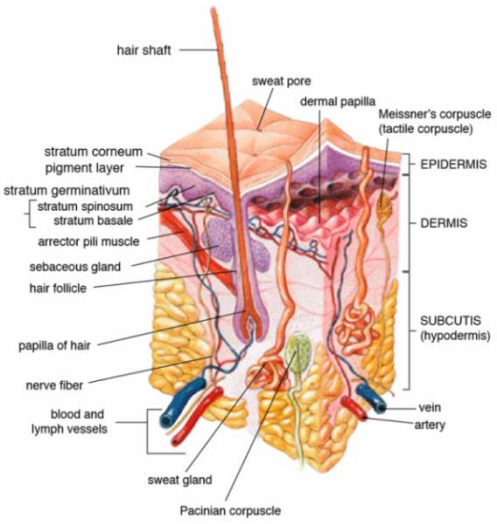

Fig. 6-1 Anatomy of the human skin.

doi:10.6342/NTU201703367

6.1.1 Experiment Setup

The experimental setup is shown in Fig. 6-2. The 3-axis force sensor is equipped on the end effector of the 7 DoF robot arm to acquire the force information and the manipulator is used to obtain its depth of indentation from the surface of human body. The robot arm executes the 1D pressing along x-axis on different kind of soft tissue to get the relationship between the reaction force and the depth of indentation of each kind of soft tissue. There are 5 subjects and all subjects are asked to lie in a massage bed. Because the massage function of the dual arm robot focuses on back, we collect the data of back to find the characteristic of soft tissue. During the 1D pressing, the robot arm moves at a constant velocity to compress the person's back until they feels pain; and then we use the collected data to analyze the soft tissue model. Previous research [21] found that different moving velocity does not affect the experimental results, so we choose 20mm/s as the velocity of moving.

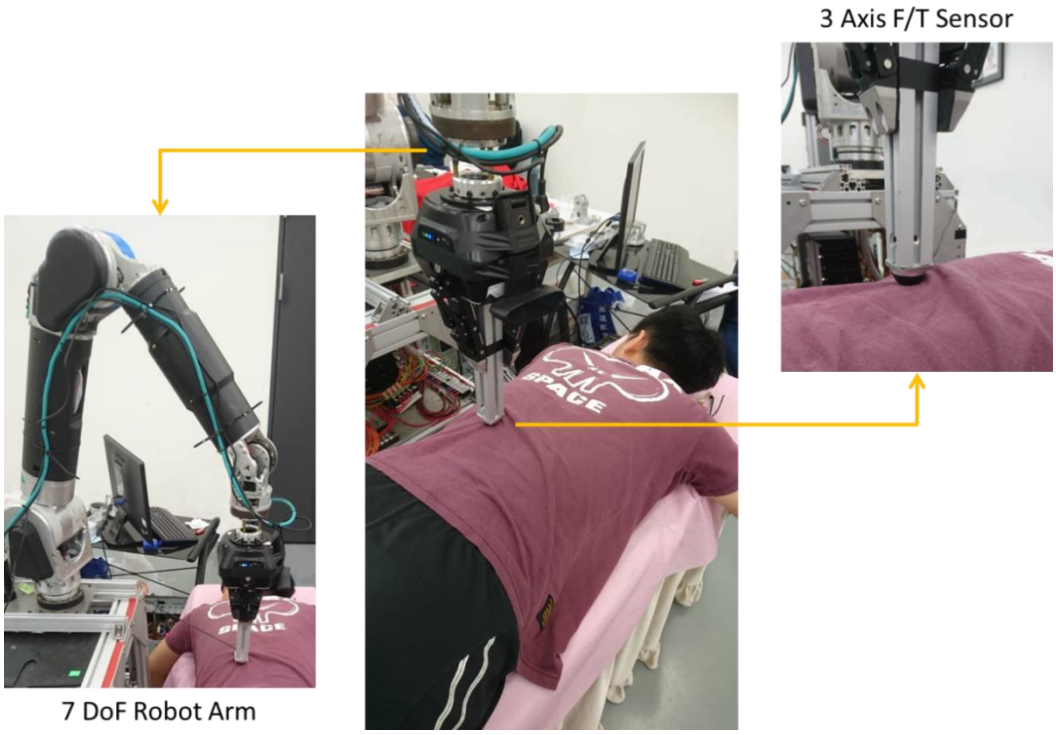

Fig. 6-2 Experiment setup of modeling of soft tissue.

doi:10.6342/NTU201703367

6.1.2 Model of Soft Tissue

Fig. 6-3 shows the experimental results of a subject with medium build. Three different parts of body are tested including soft muscle, hard muscle, and the tissue that covers bony area (noted as bone in this thesis). The indentation-force graph shows the curves which are similar to the exponential function modeled by [21]. Because we want a more intuitive model which have physical meaning and can help us know the condition of patient, we refine the soft tissue model. According to the experimental results, the force increases sharply after the indentation reaches the specified depth and we believe that it is because the end point of the manipulator has met the bone of the human body. The thickness of the soft tissue is different from person to person which should be taken into account as well. Therefore, we model the external environment force F_{ext} of impedance control as a tangent function, which is described as (6.1), where x is the depth of indentation. Then we find the approximate curve of these three indentation-force lines by curve fitting tool in MATLAB.

$$F_{ext} = \alpha tan(\beta x) \tag{6.1}$$

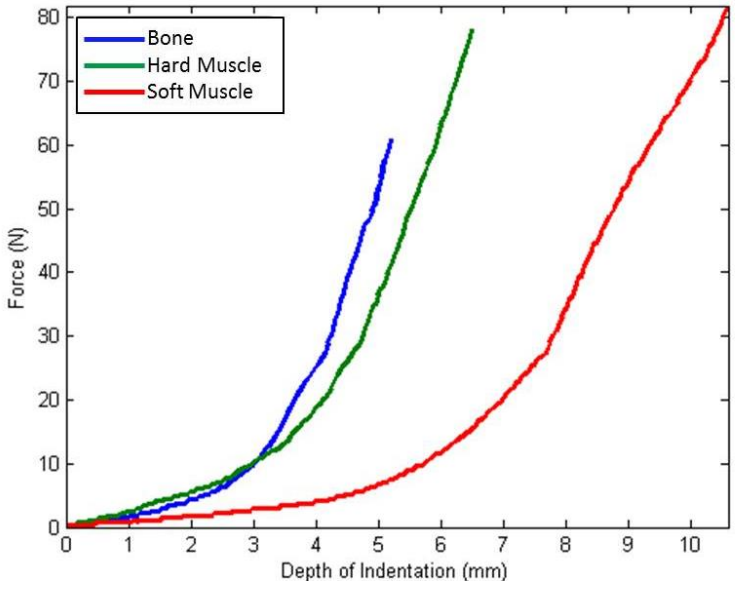

Fig. 6-3 Indentation-force graph of human body.

doi:10.6342/NTU201703367

The fitting results are shown in Table 6-1 and Fig. 6-4. The fitting indentation-force graph is displayed on top and the residual curve which presents the error between the real data and the data of fit curve is shown on bottom. The Root Mean Square Error (RMSE) of the data of soft muscle is higher because it is easy to slip when the end effect achieves the deeper depth. We notice that the hard muscle, which is hardest tissue, has the larger α than the other two parts and the tissue covering bony area which has thinnest tissue has the larger β than the others. Therefore, we deduce the following conclusion.

Soft Tissue	α	β	RMSE
Bone	4.559	0.2632	0.1896
Hard Muscle	9.786	0.1854	0.2343
Soft Muscle	4.275	0.1436	0.3936

Table 6-1 Parameters of approximate curves

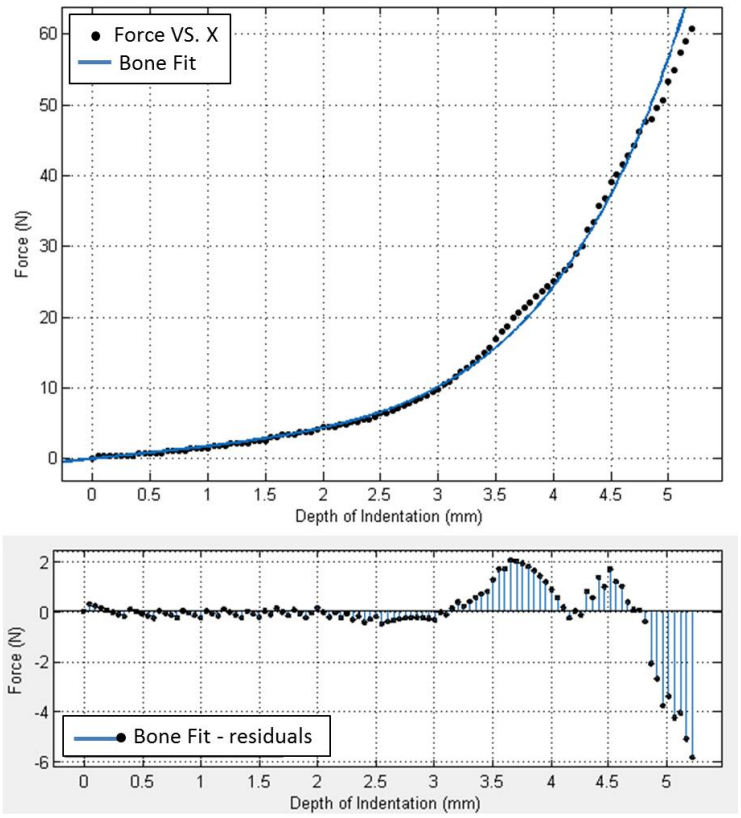

doi:10.6342/NTU201703367

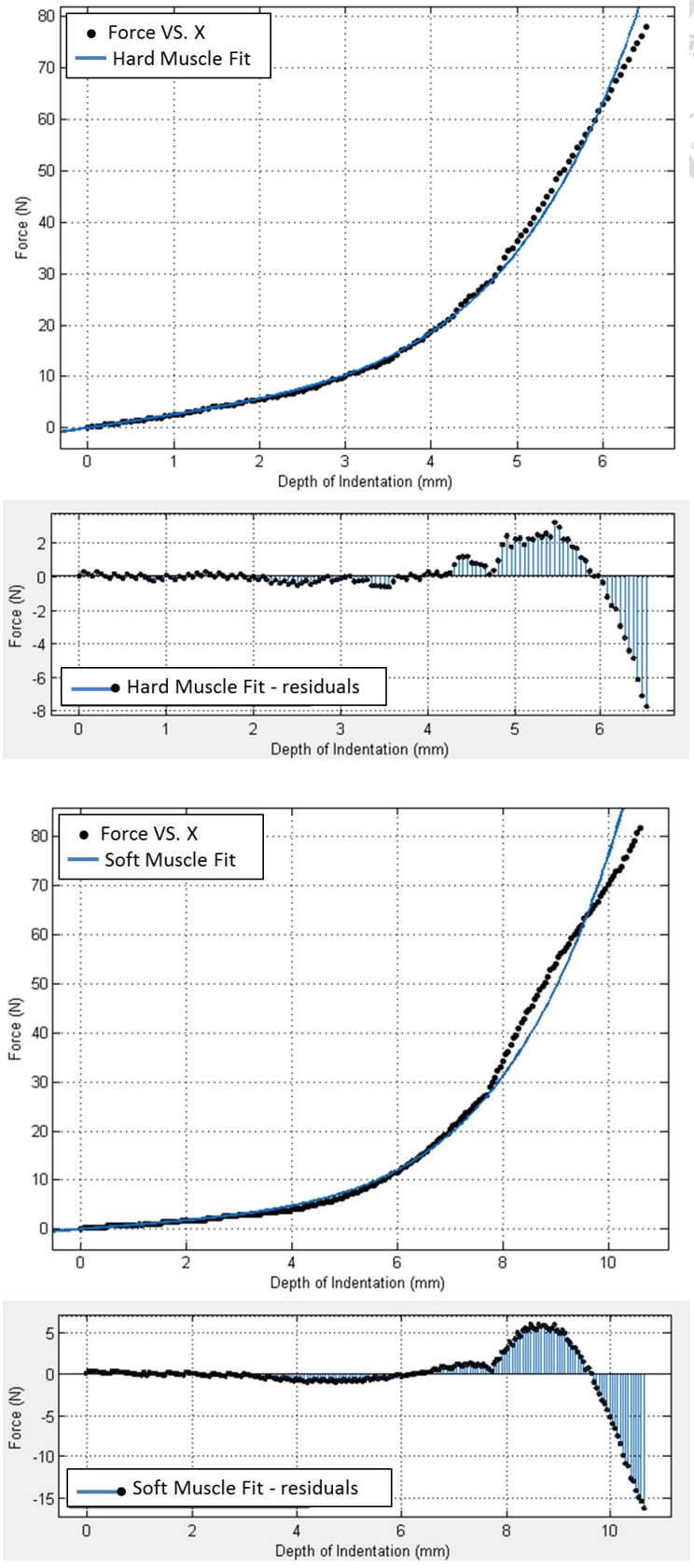

Fig. 6-4 The approximate curve of each tissue.

doi:10.6342/NTU201703367

Two parameters α and β indicate the hardness and thickness of the soft tissue. Fig. 6-5 depicts the characteristic of α and β. The parameter α represents the hardness of the soft tissue; the harder the soft tissue, the greater the parameter α. The parameter β represents the thickness of the soft tissue which varies from person to person. The thicker the soft tissue, the smaller the parameter β.

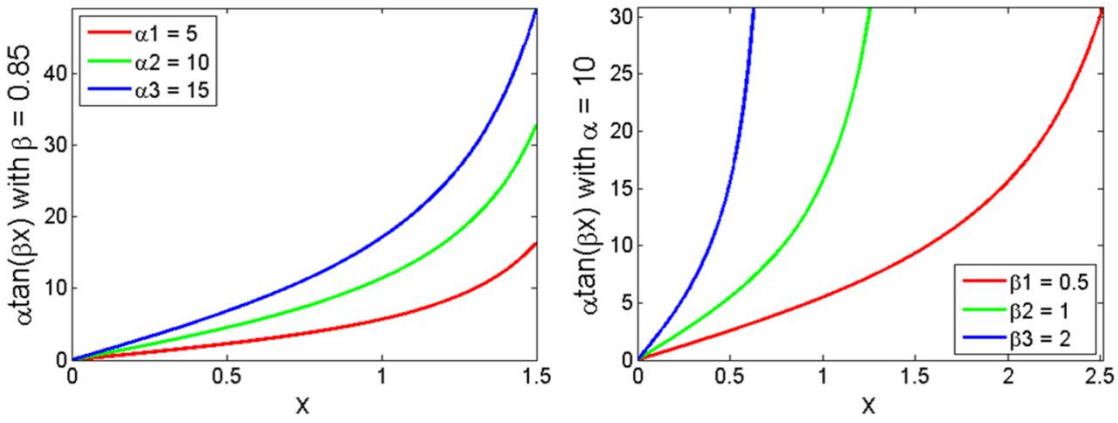

(a) α represents the hardness. (b) β represents the thickness.

Fig. 6-5 Two parameters α and β indicate the characteristic of the soft tissue.

6.2 In-Situ Tissue Stiffness Estimation

The in-situ tissue stiffness estimation algorithm we propose is based on adaptive law which can find the unknown parameters through measured input and output signals.

To estimate the tissue characteristics, the force sensor is mounted on the end effector of the robot manipulators to provide the force measurement. The Cartesian position of the force sensor is calculated by using forward kinematics. The force and position data are used as measured output and input for in-situ tissue stiffness estimation algorithm.

For in-situ tissue stiffness estimation, the function of external force should be linear. To formulate the tangent function as the type of linear algebra, the tangent

doi:10.6342/NTU201703367

function is replaced by its power series equation as (6.2).

$$tan(x) = x + \frac{x^3}{3} + \frac{2x^5}{15} \quad for \ \|x\| < \frac{\pi}{2} \tag{6.2}$$

And then, F_{ext} becomes

$$F_{ext} = \alpha(\beta x + \frac{\beta^3 x^3}{3} + \frac{2\beta^5 x^5}{15} + \cdots) \tag{6.3}$$

6.2.1 Basic Adaptive Law

In general case, the form of the parametric model is presented as (6.4). z and ϕ are signals available for measurement, θ^* is the vector with all the unknown parameters we want to estimate.

$$z = \theta^{*T}\phi \tag{6.4}$$

And the adaptive law is a differential equation as:

$$\dot{\theta}(t) = H(t)\varepsilon(t) \tag{6.5}$$

where ε is the estimation error that reflects the difference between the estimate $\theta(t)$ and θ^* (how far $\theta(t)$ is from θ^*). $H(t)$ is an adaptive gain. The object of adaptive law is to establish the conditions that guarantee that $\theta(t)$ converges to θ^* with time; on the other hand, it wants to make $|\varepsilon|$ smaller and smaller with time.

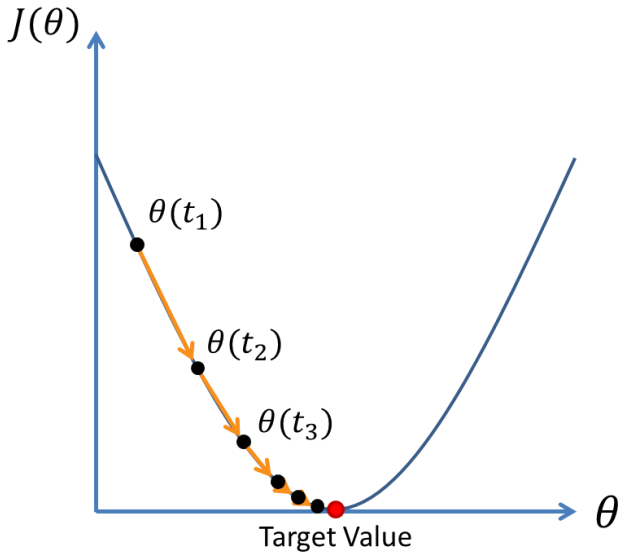

Fig. 6-6 The gradient method for adaptive law.

doi:10.6342/NTU201703367

There is an approach called gradient method (Fig. 6-6) is to update $\theta(t)$ in a direction that minimizes a certain cost of the estimation error ε. With this approach, $\theta(t)$ is adjusted in a direction that makes $|\varepsilon|$ smaller and smaller until a minimum is reached at which $|\varepsilon| = 0$ and updating is terminated.

The cost function is defined as:

$$J(\theta) = \frac{\varepsilon^2 m_s^2}{2} = \frac{(z - \theta^T \phi)^2}{2m_s^2} \tag{6.6}$$

and we minimize it with respect to θ by using the gradient method to obtain:

$$\dot{\theta} = -\gamma \nabla J(\theta) \tag{6.7}$$

where γ is the adaptive gain, $\nabla J(\theta)$ is the gradient of J with respect to θ. In this case, it can be rewritten as:

$$\nabla J(\theta) = \frac{dJ}{d\theta} = -\frac{(z - \theta^T \phi)}{m_s^2}\phi = -\varepsilon\phi \tag{6.8}$$

finally, the function of adaptive law can be written as:

$$\dot{\theta} = \gamma\varepsilon\phi,\ \theta(0) = \theta_0 \tag{6.9}$$

6.2.2 In-Situ Tissue Stiffness Estimation

According to the basic adaptive law, the parametric model of external force is constructed as (6.10) and to implement the in-situ tissue stiffness estimation.

$$F_{ext} = [\alpha\beta \quad \alpha\beta^3 \quad \alpha\beta^5]\left[x \quad \frac{x^3}{3} \quad \frac{2x^5}{15}\right]^T \tag{6.10}$$

where F_{ext} is the measured output z, x is the measured input ϕ, and α, β are unknown parameters θ^{*T}.

Because the initial error is greater, we consider the possible discounting of past data and a penalty on the initial error between the estimate θ_0 and θ^* to get the better estimation results. The recursive modified least-squares algorithm with forgetting factor is adopted as the fashion to achieve the in-situ tissue stiffness estimation. The cost

doi:10.6342/NTU201703367

function is defined as follow:

$$J(\theta) = \frac{1}{2}\int_0^t e^{-\gamma(t-\tau)} \frac{[z(\tau) - \theta^T(\tau)\phi(\tau)]^2}{m_s^2(\tau)} d\tau + \frac{1}{2} e^{-\gamma t}(\theta - \theta_0)^T Q_0 (\theta - \theta_0) \tag{6.11}$$

where the exponential term represents the forgetting factor, γ is the adaptive gain, and m_s^2 is a normalization signal. The cost function penalizes the squared error but the influence of the error is decayed with respect to the time t.

Since $\frac{z}{m_s}, \frac{\phi}{m_s} \in L_\infty$ the $J(\theta)$ is a convex function of θ at each time t, the local minimum as well as the global minimum is found at $\nabla J(\theta) = 0$, and is derived as (6.12).

$$\nabla J(\theta) = e^{-\gamma t} Q_0(\theta - \theta_0) - \int_0^t e^{-\gamma(t-\tau)} \frac{z(\tau) - \theta^T(t)\phi(\tau)}{m_s^2(\tau)} \phi(\tau) d\tau = 0 \tag{6.12}$$

From (6.12), it yields the nonrecursive least-squares algorithm as:

$$\theta(t) = P(t)[e^{-\gamma t} Q_0 \theta_0 + \int_0^t e^{-\gamma(t-\tau)} \frac{z(\tau)\phi(\tau)}{m_s^2(\tau)} d\tau] \tag{6.13}$$

where

$$P(t) = \left[e^{-\gamma t} Q_0 + \int_0^t e^{-\gamma(t-\tau)} \frac{\phi(\tau)\phi^T(\tau)}{m_s^2(\tau)} d\tau \right]^{-1} \tag{6.14}$$

In (6.14), $Q_0 = Q_0^T > 0$, and $\phi(\tau)\phi^T(\tau)$ is positive semidefinite, which implies the inverse of P exists at each time t. Therefore, the derivative of the identity matrix $I = PP^{-1}$ is derived as (6.15).

$$\frac{d}{dt} PP^{-1} = \dot{P}P^{-1} + P\frac{d}{dt}P^{-1} = 0 \tag{6.15}$$

The recursive least-squares algorithm with forgetting factor is formulated as:

doi:10.6342/NTU201703367

$$\dot{\theta} = P\varepsilon\phi, \theta(0) = \theta_0 \tag{6.16}$$

$$\dot{P} = \gamma P - P\frac{\phi\phi^T}{m_s^2}P,\ P(0) = P_0 = Q_0^{-1} \tag{6.17}$$

Then we can update θ through the integral of $\dot{\theta}$ and find the parameters α and β in the equation to estimate the characteristic of soft tissue.

6.3 Simulation and Experiment

To implement the in-situ tissue stiffness estimation on the dual arm robot for practical application, we first do the simulation to preliminarily verify its feasibility; then we make the dual arm robot execute pressing massage on subjects and estimate the characteristics of their soft tissue.

Here we take the force F_{ext} which is exerted on different kinds of soft tissue and the displacement x of the end effector to estimate the value of α and β. According to the theory of impedance control which we apply to the dual arm robot, we can derive the relationship between the action force by manipulator and the reaction force by soft tissue as follow:

$$F_{ext} = M_e\ddot{\tilde{x}} + D_e\dot{\tilde{x}} + K_e\tilde{x} = \alpha tan(\beta x) \tag{6.18}$$

where $\tilde{x} = x - x_0$. The left equation represents the model of impedance control and the right equation is the model of soft tissue.

To save the time of convergence, we adjust the trajectory and the force $F_{pressing}$ of pressing technique as (6.19) which can make sure ϕ is persistently exciting.

$$F_{pressing}(x_v, t) = F_{ext}(x_v)\Omega(t) \tag{6.19}$$

where x_v is the virtual target point, $F_{ext}(x_v)$ represents the amplitude in periodical movement. $\Omega(t)$ as defined in (6.20) is the sine function that determines the pressing

doi:10.6342/NTU201703367

time and the indentation speed.

$$\Omega(t) = |sin(\omega t)| \tag{6.20}$$

where ω represents the pressing frequency. We take absolute value to make sure the movement is along positive axis.

6.3.1 Simulation

In simulation, we assume M_e, D_e, and K_e are fixed values which are selected by [26] and the target displacement x_0 as below:

$$M_e = 1kg, K_e = 100N/m, D_e = 2 \times 0.7\sqrt{M_e D_e}\, Ns/m$$

$$x_0(t) = 5mm|sin(3\pi t)|$$

where $x_0(t)$ is the movement of pressing which has the amplitude 5mm and the pressing frequency 1.5times/s. The duration of simulation is 45secs.

We can solve (6.18) and find the real displacement x by Runge-Kutta method [39] as (6.21) which is a numerical method for ordinary differential equations. After getting x, we substitute x into $\alpha tan(\beta x)$ that α, β are known as the values to get the force F_{ext} and take them as measured input and output.

$$Initial\ value\ problem\colon\ \dot{y} = f(t, y), y(t_0) = y_0$$

$$y_{n+1} = y_n + \frac{h}{6}(k_1 + k_2 + k_3 + k_4)$$

$$k_1 = f(t_n, y_n)$$

$$k_2 = f\left(t_n + \frac{h}{2}, y_n + \frac{h}{2}k_1\right) \tag{6.21}$$

$$k_3 = f\left(t_n + \frac{h}{2}, y_n + \frac{h}{2}k_2\right)$$

$$k_4 = f(t_n + h, y_n + hk_3)$$

$$for\ n = 0, 1, 2, 3 \cdots$$

doi:10.6342/NTU201703367

where y is an unknown function of time t which we want to approximate, h is the size of the interval. The next value y_{n+1} is determined by the present value y_n and the weighted average of four increments. Each increment is the product of h and an estimated slope specified by function f.

From adaptive estimation, we will get $\alpha\beta$, $\alpha\beta^3$, and $\alpha\beta^5$. We divide $\alpha\beta^3$ by $\alpha\beta$ to obtain β^2 and its square root is β. Then the value of α can be get from $\alpha\beta$.

The results of simulation are shown in Fig. 6-7. The red one is α and the blue one is β. We test lots of adaptive gain to get the better results and find 5 is the best value for the simulation. All of them are estimated accurately.

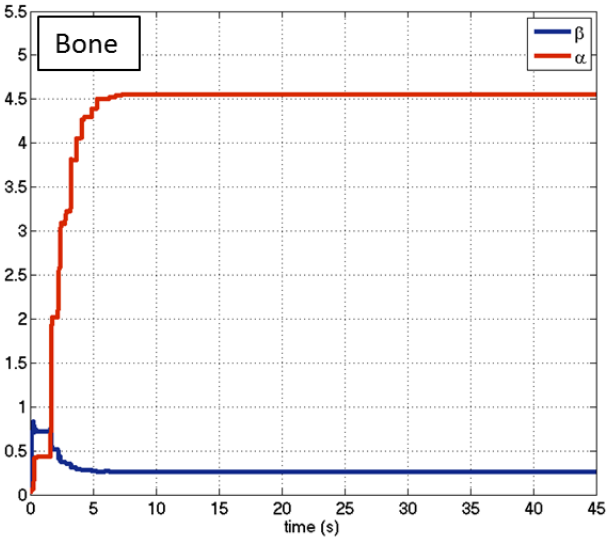

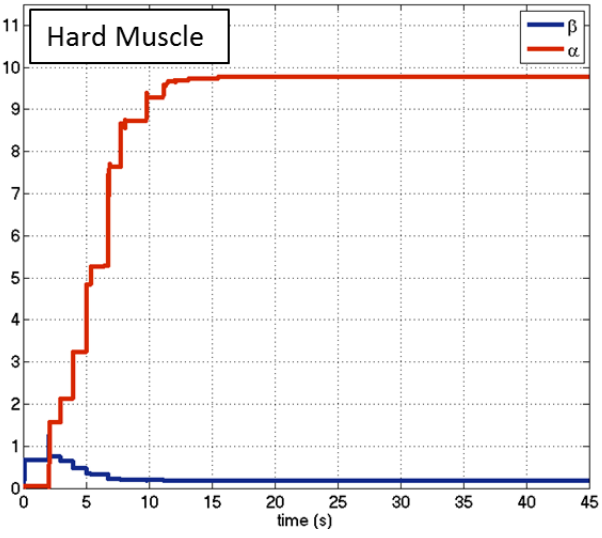

doi:10.6342/NTU201703367

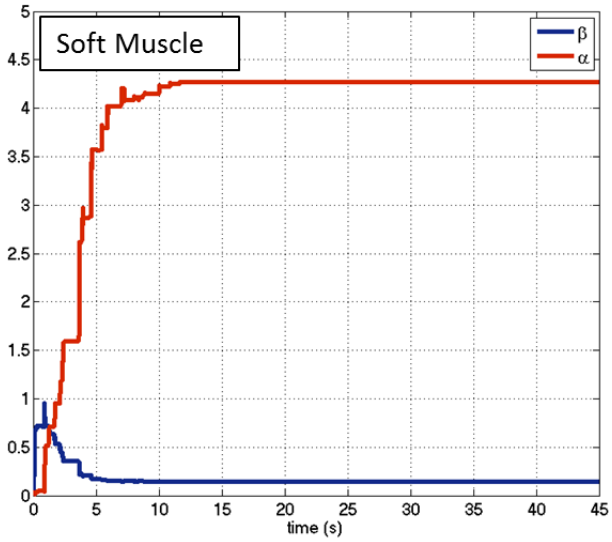

Fig. 6-7 The simulation results of each tissue.

The value of α and β of the tissue that covers bony area (noted as bone) converge in 10s and them of hard muscle and soft muscle converge in 20s.

6.3.2 Experiment

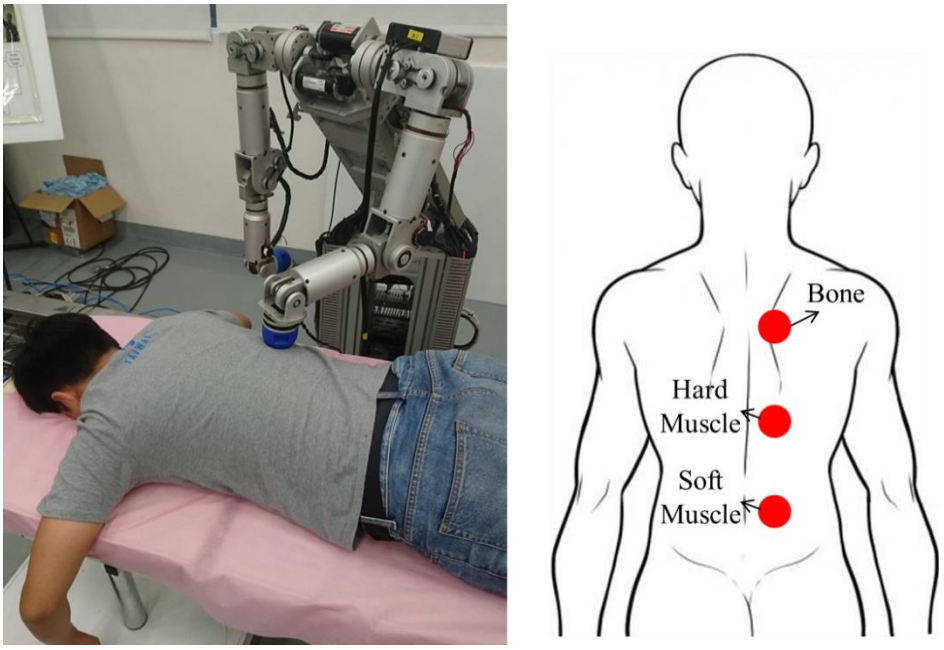

(a) (b)

Fig. 6-8 Experiment Setup. (a) The dual arm robot executes pressing on subject. (b) The points that indicate the positions we test.

doi:10.6342/NTU201703367

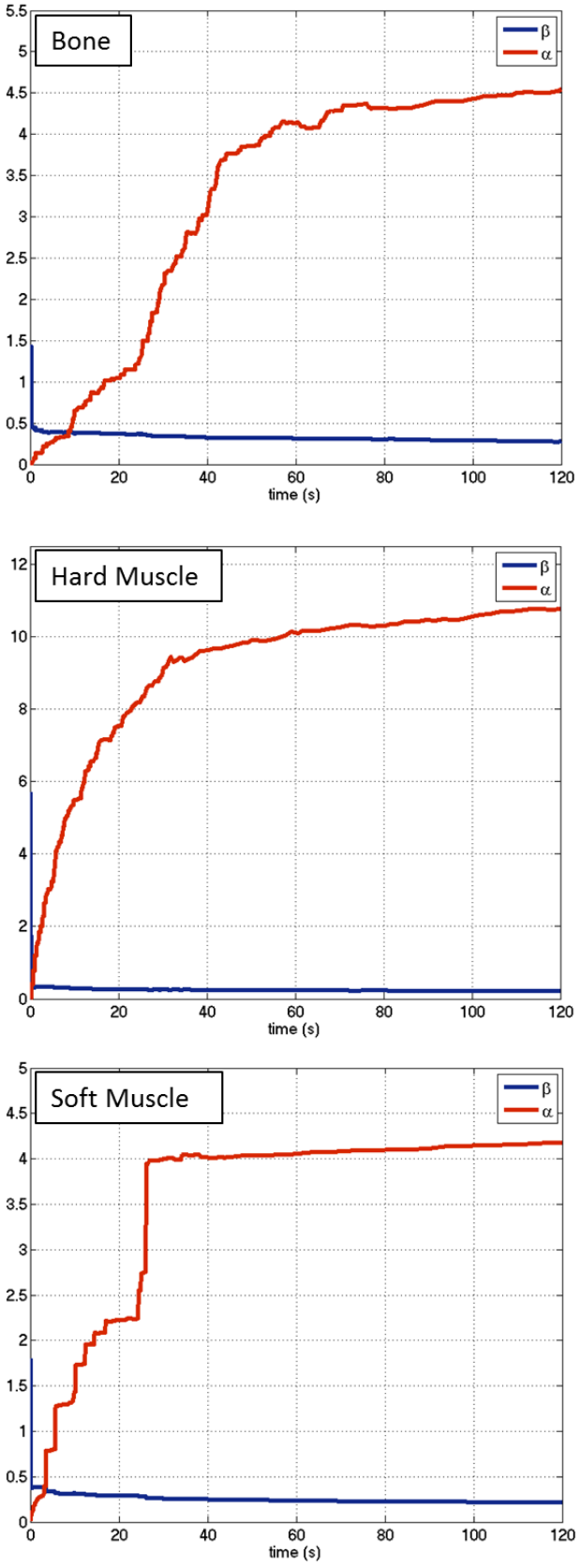

Fig. 6-9 The experimental results of subject #1.

doi:10.6342/NTU201703367

Fig. 6-9 shows the experimental results of subject #1 (the person in Fig. 6-8(a)) with medium build and Fig. 6-10 displays the displacement x and the F_{ext} extracted from his tissue, which covers bony area, in first 10secs. The values converge in 1 minute. Its convergence speed is slower than the simulation. This is because the real signal has lot of noise and the adaptive gain cannot be a large number as in simulation. Finally, we choose 0.1 as the adaptive gain.

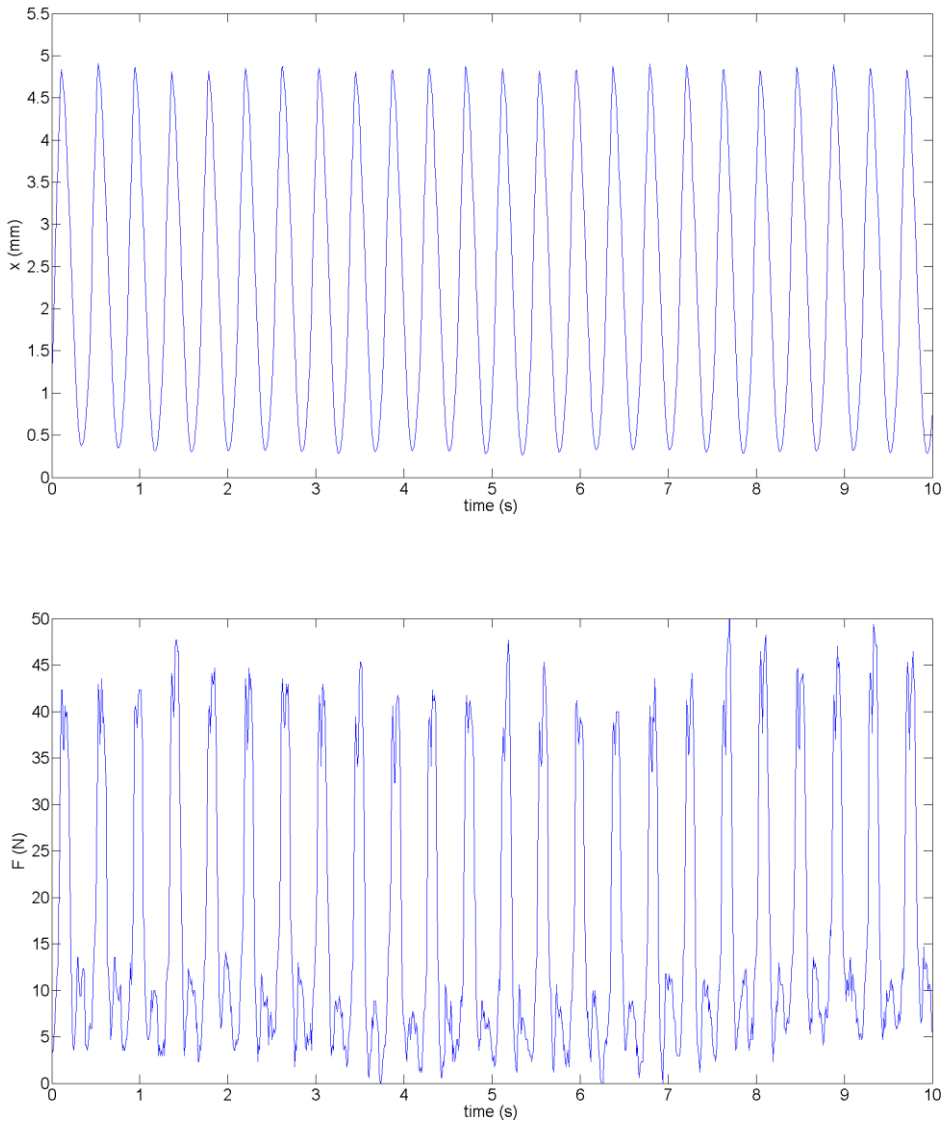

Fig. 6-10 The signals extract from subject #1.

The estimation results of 7 subjects with difference body size are shown in Table

doi:10.6342/NTU201703367

6-2. (B=Bone, H=Hard Muscle, S=Soft Muscle) The results of subject #1 are very similar with the values from the soft tissue modeling experiment. Their trends are the same but the value of soft muscle is much larger than the value we obtain in advance. The possible reason is that when the robot performs a massage, the position it touches is closer to the pelvis than the position in the previous experiment. Therefore, the thickness of soft muscle becomes thinner.

Subject	Gender	Body Shape	BMI	Body Fat (%)	B (α)	B (β)	H (α)	H (β)	S (α)	S (β)
1	male	medium	23	17.8	4.54	0.27	10.76	0.22	4.17	0.21
2	male	slim	17	12.3	5.14	0.27	11.61	0.25	4.42	0.24
3	male	hefty	30	25.7	4.40	0.23	6.00	0.22	4.08	0.19
4	female	medium	19	23.9	4.13	0.27	6.36	0.26	4.10	0.25
5	male	medium	22	16.5	4.80	0.27	12.08	0.23	4.24	0.22
6	male	slim	15	9.7	5.11	0.27	11.30	0.25	4.12	0.25
7	male	hefty	25	21.7	4.31	0.25	6.84	0.22	4.10	0.19

Table 6-2 Estimation results of 7 subjects

Subject #2 (Fig. 6-11(a)) and subject #3 (Fig. 6-11(b)) are a slim male and a hefty male respectively. From their results, we can determine that the body size will greatly affect the magnitude of α and β. Subject #2 has larger α and larger β than subject #1 because his body fat is low and the thickness of his soft tissue is relatively thinner; on the other hand, subject #3 has a smaller α and smaller β than subject #1 due to his higher body fat. Although this phenomenon may cause confusion when judging the kind of soft tissue where the robot is pressing during massage, we can add some additional

doi:10.6342/NTU201703367

criteria according to BMI or body fat percentage and use this characteristic as the judging criteria of body condition instead. The results of subject #4 (Fig. 6-11(c)) show that the female has lager β but much smaller α because of the lack of muscle and show the possibility of gender distinction by our method. Fig. 6-12 plots the estimation results of 4 subjects who have considerable size differences. The blue line represents the tissue which covers bony area (noted as bone), the green line represents hard muscle, and the red line represents soft muscle.

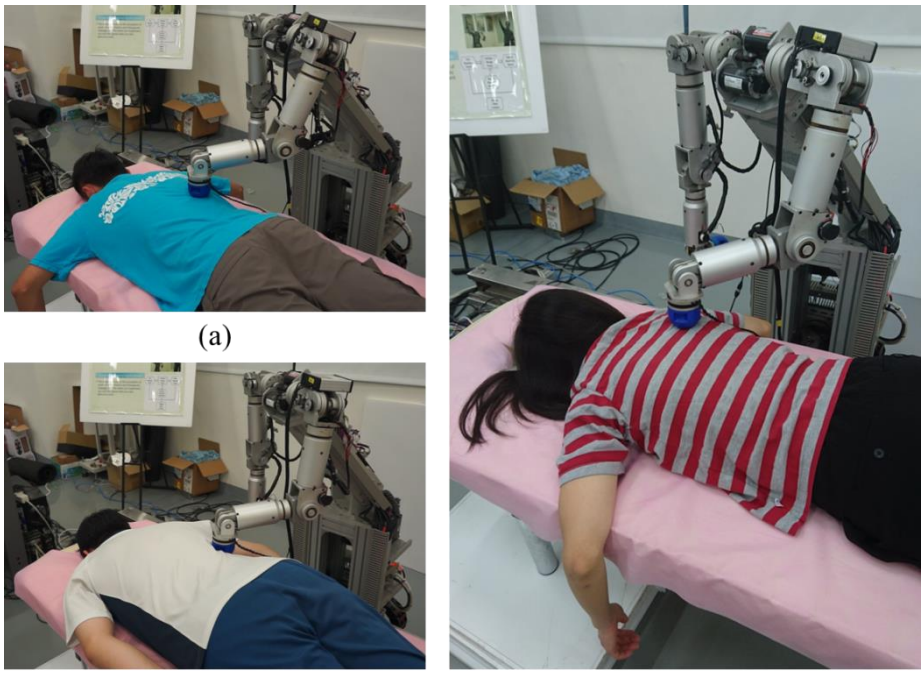

Fig. 6-11 The subjects with differences. (a) Subject #2 (b) Subject #3 (c) Subject #4

The estimation results verify the in-situ tissue stiffness estimation method we propose can successfully estimate the hardness and the thickness of the soft tissue during robotics massage.

doi:10.6342/NTU201703367

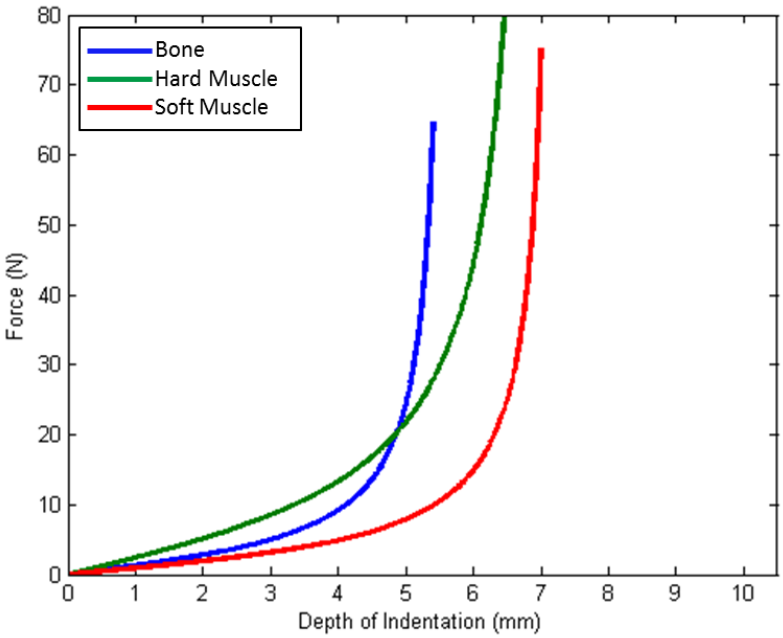

(a) Subject #1 (male-medium)

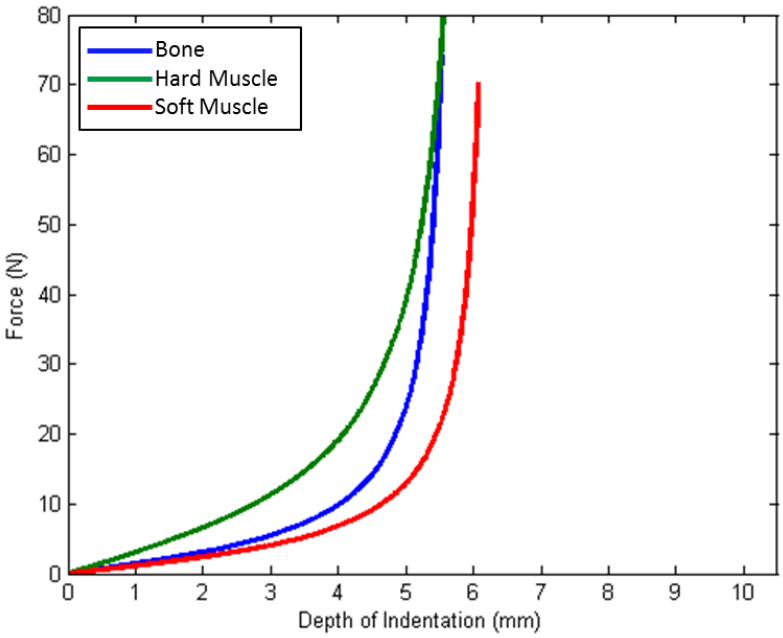

(b) Subject #2 (male-slim)

doi:10.6342/NTU201703367

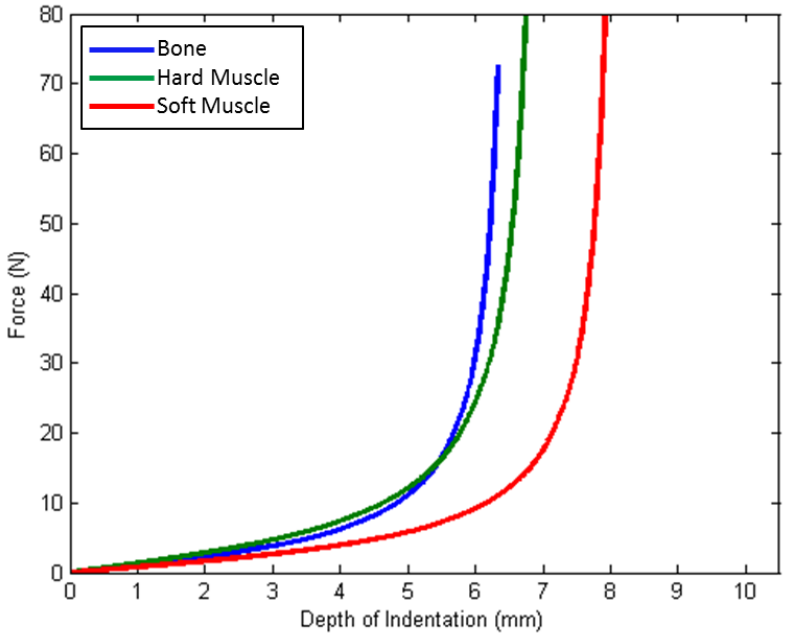

(c) Subject #3 (male-hefty)

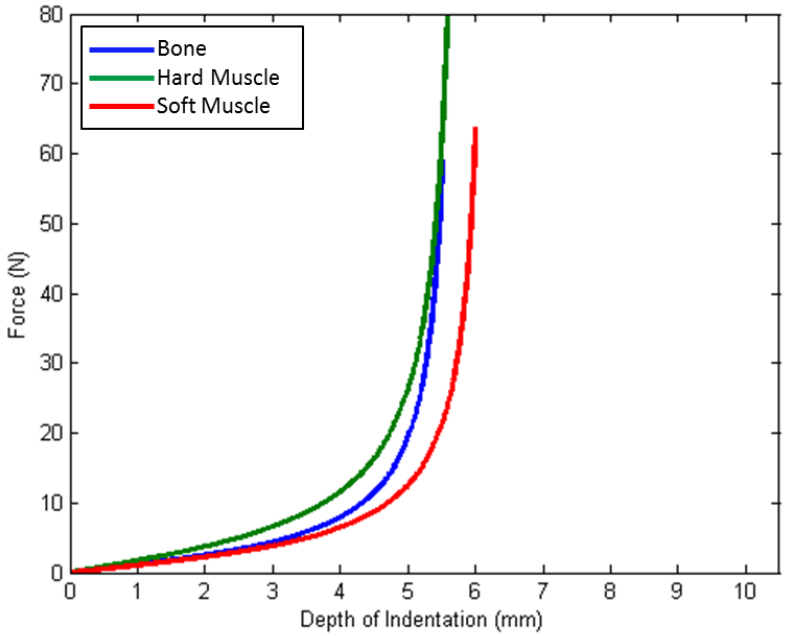

(d) Subject #4 (female-medium)

Fig. 6-12 The estimation results of 4 subjects who have considerable size differences. (a) Subject #1 (b) Subject #2 (c) Subject #3 (d) Subject #4

doi:10.6342/NTU201703367

Chapter 7 Conclusions and Future Work

7.1 Conclusions

In this thesis, we successfully adopt the anthropomorphic dual arm robot developed in our lab to implement robotics therapeutic massage. The Cartesian space impedance control and joint impedance control which are capable of providing desired force for massage are apply to the dual arm robot. Then the robotics therapeutic massage system is endowed with a variety of massage techniques based on impedance control.

The two main problems of the robotics therapeutic massage are successfully solved. To make the robot autonomously generate adaptive massage trajectory which is individual person specific by using a low-cost sensor, we developed a low-cost laser range finder (LRF) based on triangulation and laser line scanner module. The LRF can extract the 3D model with a single scan which is more convenient for massage trajectory planning. Because all components are commercial products bought online, its cost is less than 10% of the price of the commercial product. To prove the performance of our LRF, the distance measurement experiment is presented which take the Hokuyo LRF as ground truth. All error rates are below 0.75% which means our module has comparable performance as the commercial product.

For adaptive massage trajectory generation, we propose a method based on features of human back and morphing algorithm. We first construct the standard 3D model which indicates the acupressure points of general human back, and then extract the back contours of the standard 3D model and subject by human back feature extraction. After getting the contour, we map the standard 3D model on the back of the subject using the

doi:10.6342/NTU201703367

morphing algorithm to find the acupressure points and generate the adaptive trajectories for pressing, rubbing, and stroking. In the experiment, we compare the results from the method we propose with the real acupressure points which are defined by a massage therapist in advance. The experimental results show that the average distance error of the acupressure points from ten subjects is smaller than the contact radius of the sphere-shaped end-effector which means our algorithm can precisely generate adaptive trajectory for different people and can be applied in practical applications. The trajectories of rubbing and stroking are presented as well. Finally, we successfully apply the self-developed LRF and the adaptive trajectory generation algorithm to the dual robot for massage. Our method saves more than half the time needed with teach and play.

In order to let the robot estimate the characteristics of soft tissue during massage for appropriate physical human-robot interaction and providing more friendly service, we figure out the characteristics of soft tissue by using a 7 DoF robot arm and build an intuitive soft tissue model which have the information of hardness and thickness. Then we present an in-situ tissue stiffness estimation method which can estimate the characteristics of patient's soft tissue during massage. This estimation method is based on recursive least-squares algorithm with forgetting factor which is one algorithm of the adaptive law. We adopt the force exerted on soft tissue and the movement of the robot manipulator as measured output and input signals in the algorithm. In the experiment, the robot estimates 3 kinds of soft tissue form 7 subjects with different body size during pressing massage. The experiment illustrates the estimation results have the same trend as the characteristics of the model we propose and we can use the estimation results as the judging criteria of body condition.

doi:10.6342/NTU201703367

The main contributions of this thesis are listed below:

1. We develop a 3D low-cost laser range finder whose components are bought online and it cost is less than 10% of the price of the commercial product.
2. We propose a method that can accurately generate adaptive massage trajectory which is individual person specific based on features of human back and morphing algorithm. The massage trajectories include pressing, rubbing, and stroking.
3. We successfully apply the LRF and adaptive massage trajectory generation to robotics therapeutic massage, which are upper back massage and full body massage.
4. We explore the characteristics of soft tissue and propose intuitive model of soft tissue as a tangent function which can indicate the hardness and thickness of soft tissue.
5. We propose a method that can accurately estimate the characteristics of patient's soft tissue during massage based on adaptive law, the force exerted on soft tissue, and the movement of the robot manipulator.

7.2 Future Work

Our goal is to make the LRF more suitable for small robotics applications, and preliminary technologies. We are keeping trying to minimize the volume of the LRF while improve its accuracy and change the light source to near infrared ray to give the user a more comfortable sensory experience. We will also try to use the standard model in 3D space directly rather than project it in 2D to get the better performance. The standard 3D model for different pose is determined by us currently. We will add human pose estimation we proposed previously [40] to estimate the subjects' pose and

doi:10.6342/NTU201703367

autonomously find the suitable standard 3D model for them.

In the future, we will combine the in-situ tissue estimation with control strategies to make the control system more stable and will dynamically change the time of massage and the massage technique according to the characteristic of soft tissue.

doi:10.6342/NTU201703367

References

[1] T. Mukai, S. Hirano, M. Yoshida, H. Nakashima, Shijie Guo and Y. Hayakawa, "Whole-Body Contact Manipulation Using Tactile Information," in *IEEE/RSJ International Conference on Intelligent Robots and Systems (IROS)*, 2011, pp. 2445-2451.

[2] X. Papageorgiou, G. Chalvatzaki, C. Tzafestas and P. Maragos, "Hidden Markov Modeling of Human Normal Gait Using Laser Range Finder for a Mobility Assistance Robot," in *IEEE International Conference on Robotics and Automation (ICRA)*, 2014, pp. 482-487.

[3] H. Gross, S. Mueller, C. Schroeter, M. Volkhardt, A. Scheidig, K. Debes, K. Richter and N. Doering, "Robot Companion for Domestic Health Assistance: Implementation, Test and Case Study Under Everyday Conditions in Private Apartments," in *IEEE/RSJ International Conference on Intelligent Robots and Systems (IROS)*, 2015, pp. 5992-5999.

[4] Y. Huang, P. Soueres and J. Li, "Contact Dynamics of Massage Compliant Robotic Arm and Its Coupled Stability," in *IEEE International Conference on Robotics and Automation (ICRA)*, 2014, pp. 1499-1504.

[5] Y. Huang, J. Li, Q. Huang and C. Liu, "Design and Control of Anthropomorphic BIT Soft Arms for TCM Remedial Massage," in *IEEE/RSJ International Conference on Intelligent Robots and Systems (IROS)*, 2013, pp. 1960-1965.

[6] T. Ando, M. Takeda, T. Maruyama, Y. Susuki, T. Hirose, S. Fujioka, O. Mizuno, K. Yamada, Y. Ohno and H. Yukio, "Biosignal-Based Relaxation Evaluation of

doi:10.6342/NTU201703367

Head-Care Robot," in *35th Annual International Conference of the IEEE Engineering in Medicine and Biology Society (EMBC)*, 2013, pp. 6732-6735.

[7] R. C. Luo, C. Chang and Yi-Wen Perng, "Impedance Control on a Multi-Fingered Robot Hand Based on Analyzed Electromyographic Information for Massage Applications," in *IEEE International Symposium on Industrial Electronics*, 2009, pp. 1228-1233.

[8] R. C. Luo and C. Chang, "Electromyographic Signal Integrated Robot Hand Control for Massage Therapy Applications," in *IEEE/RSJ International Conference on Intelligent Robots and Systems (IROS)*, 2010, pp. 3881-3886.

[9] R. C. Luo, C. Hsu and S. Chen, "Electroencephalogram Signal Analysis as Basis for Effective Evaluation of Robotic Therapeutic Massage," in *IEEE/RSJ International Conference on Intelligent Robots and Systems (IROS)*, 2016, pp.2940-2945.

[10] K. C. Jones, and W. Du, "Development of a Massage Robot for Medical Therapy," in *2003 IEEE/ASME International Conference on Advanced Intelligent Mechatronics (AIM)*, 2003, pp. 1096-1101.

[11] C. King, T. Chen, A. Jain and C. Kemp, "Towards an Assistive Robot that Autonomously Performs Bed Baths for Patient Hygiene," in *IEEE/RSJ International Conference on Intelligent Robots and Systems (IROS)*, 2010, pp. 319-324.

[12] L. Shouyin, G. Huanbing, L. Cungen and W. Tao, "Design of Chinese Medical Massage Robot System," in *International Conference on Electrical and Control Engineering*, 2011, pp. 3882-3885.

doi:10.6342/NTU201703367

[13] Chih-Cheng Peng, Thong-Shing Hwang, Chih-Jui Lin, Yao-Ting Wu, Ching-Yi Chang and Jian-Bin Huang, "Development of Intelligent Massage Manipulator and Reconstruction of Massage Process Path Using Image Processing Technique," in *IEEE Conference on Robotics, Automation and Mechatronics*, 2010, pp. 551-556.

[14] Y. Wei, K. Gu, X. Cui, C. Hao, H. Wang and Y. Chang, "Strategies for Feet Massage Robot to Position the Pelma Acupoints with Model Predictive and Real-Time Optimization," *International Journal of Control, Automation and Systems, vol. 14, no. 2,* pp. 628-636, 2016.

[15] H. Chen, X. Wu, W. Feng, T. Xu and Y. He, "Design and Path Planning of Massagebot: One Massaging Robot Climbing Along the Acupuncture Points," in *IEEE International Conference on Information and Automation (ICIA)*, 2016, pp. 969-973.

[16] R. C. Luo, S. Y. Chen, and K. C. Yeh, "Human Body Trajectory Generation Using Point Cloud Data for Robotics Massage Applications," in *2014 IEEE International Conference on Robotics and Automation (ICRA)*, 2014, pp. 5612-5617.

[17] K. Buys, C. Cagniart, A. Baksheev, T. De Laet, J. De Schutter and C. Pantofaru, "An Adaptable System for RGB-D Based Human Body Detection and Pose Estimation," *Journal of Visual Communication and Image Representation, vol. 25, no. 1,* pp. 39-52, 2014.

[18] K. Konolige, J. Augenbraun, N. Donaldson, C. Fiebig and P. Shah, "A Low-Cost Laser Distance Sensor," in *IEEE International Conference on Robotics and Automation (ICRA)*, 2008, pp. 3002-3008.

[19] X. Chen, M. Zhao, L. Xiang, F. Sugai, H. Yaguchi, K. Okada and M. Inaba,

doi:10.6342/NTU201703367

"Development of a Low-Cost Ultra-Tiny Line Laser Range Sensor," in *IEEE/RSJ International Conference on Intelligent Robots and Systems (IROS)*, 2016, pp. 111-116.

[20] E. Chen, J. Novakofski, W. Jenkins and W. O'Brien, "Young's Modulus Measurements of Soft Tissues with Application to Elasticity Imaging," *IEEE Transactions on Ultrasonics, Ferroelectrics and Frequency Control, vol. 43, no. 1,* pp. 191-194, 1996.

[21] L. Hu, J. Zhang, C. Li, Y. Cui and L. Wang, "A Force-Position Control System Based on Soft Tissue under Large Deformation," *Advances in Mechanical Engineering, vol. 5, no. 0,* pp. 1-8, 2013.

[22] C. Yeh, F. Su, I. Goryacheva, Y. Martynenko, M. Dosaev and M. Ju, "Image-Assisted Method for Estimating Local Stiffness of Soft Tissues and Calibration of Bias Due to Aqueous Humor Effect," *Sensors and Actuators A: Physical, vol. 212,* pp. 42-51, 2014.

[23] A. Yakovenko, I. Goryacheva and M. Dosaev, "Estimating Characteristics of a Contact Between Sensing Element of Medical Robot and Soft Tissue," in *New Trends in Mechanism and Machine Science,* 2016, pp. 561-569.

[24] V. Golovin, M. Arkhipov and V. Zhuravlev,, "Force Training for Position/Force Control of Massage Robots," in *New Trends in Medical and Service Robots*, 2014, pp. 95-107.

[25] A. Leskov, V. Golovin, M. Arkhipov and L. Kocherevskaya, "Training of Robot to Assigned Geometric and Force Trajectories," in *New Trends in Medical and Service Robots*, 2016, pp. 75-84.

doi:10.6342/NTU201703367

[26] C. Ott, R. Mukherjee and Y. Nakamura, "A Hybrid System Framework for Unified Impedance and Admittance Control," *Journal of Intelligent & Robotic Systems, vol. 78, no. 3-4*, pp. 359-375, 2014.

[27] C. Ott, R. Mukherjee and Y. Nakamura, "Unified Impedance and Admittance Control," in *IEEE International Conference on Robotics and Automation*, 2010, pp. 554-561.

[28] K. Mouri, K. Terashima, P. Minyong, H. Kitagawa, and T. Miyoshi, "Identification and Hybrid Impedance Control of Human Skin Muscle by Multi-fingered Robot Hand," in *2007 IEEE/RSJ International Conference on Intelligent Robots and Systems*, 2007, pp. 2895-2900.

[29] "Harmonic Drive," [Online]. Available: https://en.wikipedia.org/wiki/Harmonic_drive. [Accessed 12 7 2017].

[30] "RTOS Platform," Interval Zero, [Online]. Available: http://www.intervalzero.com/. [Accessed 12 7 2017].

[31] N. Hogan, "Impedance Control: An Approach to Manipulation," in *American Control Conference*, 1984, pp. 304-313.

[32] R. C. Luo, H. B. Huang, C. Y. Yi, and Y. W. Perng, "Adaptive Impedance Control for Safe Robot Manipulator," in *2011 9th World Congress on Intelligent Control and Automation (WCICA)*, 2011, pp. 1146-1151.

[33] "Laser Safety Manual," Old Dominion University, [Online]. Available: https://www.odu.edu/content/dam/odu/offices/environmental-health-safety/docs/laser-safety-manual.pdf. [Accessed 12 7 2017].

[34] "Self-Made Low-Cost 3D Laser Scanner (3D Laser Radar)," Csksoft.net, [Online].

doi:10.6342/NTU201703367

Available: http://www.csksoft.net/blog/post/lowcost_3d_laser_ranger_1.html. [Accessed 12 7 2017].

[35] "Hokuyo URG-04LX Laser Range Finder," Hokuyo, [Online]. Available: https://www.hokuyo-aut.jp/search/single.php?serial=165. [Accessed 12 7 2017].

[36] T. Beier and S. Neely, "Feature-Based Image Metamorphosis," *ACM SIGGRAPH Computer Graphics*, pp. 35-42, 1992.

[37] "Chinese Medicine Theory Site," Yin Yang Hous, [Online]. Available: https://theory.yinyanghouse.com/. [Accessed 12 7 2017].

[38] "Subcutaneous tissue," [Online]. Available: https://en.wikipedia.org/wiki/Subcutaneous_tissue. [Accessed 12 7 2017].

[39] "Runge–Kutta methods," [Online]. Available: https://en.wikipedia.org/wiki/Runge%E2%80%93Kutta_methods. [Accessed 12 7 2017].

[40] R. C. Luo and S. Chen, "Human Pose Estimation in 3-D Space Using Adaptive Control Law With Point-Cloud-Based Limb Regression Approach," *IEEE Transactions on Industrial Informatics, vol. 12, no. 1,* pp. 51-58, 2016.

doi:10.6342/NTU201703367

VITA

姓名: 唐莉彤

性別: 女

生日: 08.12.1993

籍貫: 台北

學歷:

民國 106 年 國立台灣大學電機工程學研究所畢業

民國 104 年 國立交通大學光電工程學系畢業

民國 100 年 台北市立內湖高級中學畢業

榮譽事蹟:

民國 105 年 參加「PMC 工業機器人智慧應用創意競賽」榮獲團體組 **冠軍**

doi:10.6342/NTU201703367